

Oscillating dynamical friction on galactic bars by trapped dark matter

Rimpei Chiba¹^{*} and Ralph Schönrich²

¹*Rudolf Peierls Centre for Theoretical Physics, Clarendon Laboratory, Parks Road, Oxford OX1 3PU, UK*

²*Mullard Space Science Laboratory, University College London, Holmbury St. Mary, Dorking, Surrey, RH5 6NT, UK*

Accepted XXX. Received YYY; in original form ZZZ

ABSTRACT

The dynamic evolution of galactic bars in standard Λ CDM models is dominated by angular momentum loss to the dark matter haloes via dynamical friction. Traditional approximations to dynamical friction are formulated using the linearized collisionless Boltzmann equation and have been shown to be valid in the *fast regime*, i.e. for rapidly slowing bars. However, the linear assumption breaks down within a few dynamical periods for typical slowly evolving bars, which trap a significant amount of disc stars and dark matter in resonances. Recent observations of the Galactic bar imply this *slow regime*. We explore the fundamental mechanism of dynamical friction in the slow regime with analytical and test-particle methods. Here, angular momentum exchange is dominated by resonantly trapped orbits which slowly librate around the resonances. In typical equilibrium haloes, the initial phase-space density within the trapped zone is higher at lower angular momentum. Since the libration frequency falls towards the separatrix, this density contrast winds up into a phase-space spiral, resulting in a dynamical friction that oscillates with \sim Gyr periods and damps over secular timescales. We quantify the long-term behaviour of this torque with secular perturbation theory, and predict two observable consequences: i) The phase-space spirals may be detectable in the stellar disc where the number of windings encodes the age of the bar. ii) The torque causes oscillations in the bar’s pattern speed overlaying the overall slowdown – while not discussed, this feature is visible in previous simulations.

Key words: Galaxy: kinematics and dynamics – Galaxy: evolution – methods: numerical

1 INTRODUCTION

Dark matter haloes strongly affect the evolution of galactic bars: dynamical friction transfers angular momentum and energy from the galactic bar to the dark matter halo, allowing bars to slow and grow. This angular momentum transfer depends both on the density and on the kinematic state of the dark halo. Consequently, we can constrain the otherwise poorly known phase-space distribution and nature of dark haloes from the measured slowing rate of bars.

While a wide range of numerical simulations have addressed the angular momentum transfer from bars to haloes (e.g. Hernquist & Weinberg 1992; Debattista & Sellwood 2000; Athanassoula 2003), the analytical treatment is still incomplete. Tremaine & Weinberg (1984, hereafter TW84) derived a formula of dynamical friction in an inhomogeneous spherical system using linear perturbation theory. Their formula generalises the earlier LBK torque formula (Lynden-Bell & Kalnajs 1972), which describes the angular momentum transport in two-dimensional disc galaxies. Unlike the dynamical friction in a homogeneous system (Chandrasekhar 1943), the LBK formula shows that in an inhomogeneous system, where orbits are quasi-periodic, the dominant angular momentum transfer arises from discrete resonances. TW84 also investigated the non-linear motion of orbits near resonances and showed that the LBK formula is only valid in the so-called *fast regime*. Here, fast means that the resonances sweep across the phase space of the halo rapidly

enough to preclude the growth of non-linear responses, in particular trapping at resonances. This allows the system to remain in the linear regime. Weinberg (1985) showed that the LBK torque formula predicts a strong friction on the bar, extracting most of its angular momentum in a few rotation periods. This problem was revisited by Weinberg (2004, hereafter W04), where he pointed out that the assumption of the perturbation being turned on adiabatically in the distant past (the time-asymptotic limit) is problematic since the evolution timescale of the bar is only several times the characteristic dynamical period. Relaxing this assumption enabled W04 to model the transient effect and reduce the overall torque. Yet, the W04 treatment remains restricted to the fast regime and cannot be applied to the *slow regime* where resonant trapping comes into play.

This slow regime (resonant trapping by the Galactic bar) is, however, implied by the stellar kinematics of the Solar neighbourhood observed by the *Gaia* satellite (e.g. Katz et al. 2019; Hunt et al. 2019; Monari et al. 2019; Binney 2020; Trick et al. 2021). The resonantly trapped stars manifest as stellar streams which occupy a sizeable fraction of the local phase-space volume. Modelling particularly the Hercules stream, Chiba et al. (2021) inferred that the bar is decelerating at a moderate rate keeping a good portion of local stars trapped. Furthermore, signatures of trapping is found in the metallicity distribution of local stars: the corotation resonance of the slow/long bar exhibit a monotonic increase of metallicity towards the core of the resonance, indicating a tree-ring like growth as predicted by a naturally slowing bar that sequentially captured stars from small Galactocentric radii (Chiba & Schönrich 2021).

^{*} E-mail: rimpei.chiba@physics.ox.ac.uk

Resonant trapping by the bar is also commonly seen in self-consistent N -body simulations: spectral analysis of orbits in barred galaxies shows significant clustering near resonances (e.g. [Ceverino & Klypin 2007](#)). Simulations by [Halle et al. \(2018\)](#) show that these trapped stars adhere to the resonance as the bar slows down. Some works have also discussed direct trapping of dark matter into a ‘shadow bar’ ([Athanassoula 2007](#); [Petersen et al. 2016](#); [Collier & Madigan 2021](#)).

Thus both observations and simulations indicate that bars generally evolve slowly enough to exert resonant trapping and make the formalism of TW84 and W04 inapplicable. The dynamics of this resonant trapping is best viewed in the slow angle-action plane which exhibits a phase flow akin to that of a simple pendulum: trapped orbits librate around the resonance centre (and their slow angle oscillates around the resonance midpoint) while untrapped orbits circulate above and below the separatrix (i.e. their slow angle moves freely across the whole 2π range). Before bar formation, the phase-space density typically declines towards large slow action (i.e. the z -angular momentum). When the bar forms, the trapped region grows and captures orbits from both above and below the resonance, reconnecting phase space across regions of different density. The newly trapped orbits are thus inevitably non-uniform in their libration angle distribution. As these trapped orbits librate around the resonance along contours of constant libration actions, their innate angle imbalance results in a periodic dynamical friction on the bar. However, due to the monotonic decrease of libration frequency towards the separatrix, the density inside the trapped zone gradually winds up into a phase-space spiral, and the net torque from trapped orbits slowly attenuates. The phase mixing timescale is set by the libration period (typically > 1 Gyr), which prevents complete mixing in a Hubble time. This leads us to predict that bars are subject to pattern speed oscillations on the timescale of the libration, which is an order of magnitude longer than the short-period fluctuations due to bar-spiral interactions ([Wu et al. 2016](#); [Hilmi et al. 2020](#)).

In this paper, we study this behaviour both analytically and in test particle simulations. The analytical approach uses the standard secular perturbation theory founded on the method of averaging. Our formulation is initially done for a constantly rotating bar. The resulting torque terms provide a necessary, but still incomplete step towards a fully self-consistent model where the bar slows in response to the torque by the halo. For this, one has to further address the processes of dragging by the resonance, jumping over the resonance, as well as capture into and escape from it (e.g. [Henrard 1982](#); [Sridhar & Touma 1996](#)).

This paper is organized as follows. In section 2, we introduce our model of the halo and the bar. Section 3 reviews the torque formula in the fast regime and discuss its problems when applied to systems in the slow regime. In section 4, we lay out the standard method to treat the non-linear dynamics near resonance and formulate the dynamical friction in the slow regime which we verify against test-particle simulations. We will discuss the consequence of an evolving bar in section 5 and sum up in section 6.

2 MODEL

2.1 Model of dark halo

We model the dark halo with an isotropic [Hernquist \(1990\)](#) model:

$$\rho_0(r) = \frac{M}{2\pi} \frac{r_s}{r(r_s + r)^3}, \quad (1)$$

$$\Phi_0(r) = -\frac{GM}{r_s + r}, \quad (2)$$

where G is the gravitational constant, M is the total halo mass, and r_s the halo scale radius. By default, we set $M = 1.5 \times 10^{12} M_\odot$ and $r_s = 20$ kpc. The corresponding distribution function and setup of the test-particle simulations are described in Appendix A.

2.2 Model of Galactic bar

We model the bar potential with a quadrupole rotating at pattern speed Ω_p :

$$\Phi_b(r, \vartheta, \varphi, t) = \Phi_b(r) \sin^2 \vartheta \cos 2(\varphi - \Omega_p t), \quad (3)$$

where (r, ϑ, φ) are the usual spherical coordinates. The radial dependence of the bar potential is

$$\Phi_b(r) = -\frac{Av_c^2}{2} \left(\frac{r}{r_{CR}} \right)^2 \left(\frac{b+1}{b+r/r_{CR}} \right)^5, \quad (4)$$

where A is the dimensionless strength of the bar and b describes the ratio between the bar scale length and the corotation radius r_{CR} . This potential is designed to lengthen as the bar slows. We fit our model to that of [Sormani et al. \(2015\)](#) at the Galactic plane ($\vartheta = \pi/2$) and obtain $A = 0.02$, $b = 0.28$. By default, we use the current bar pattern speed $\Omega_p = 35 \text{ km s}^{-1} \text{ kpc}^{-1} \approx 35.8 \text{ Gyr}^{-1}$ ([Binney 2020](#); [Chiba & Schönrich 2021](#); [Clarke & Gerhard 2021](#)).

2.3 Angle-action variables in spherical potential

The description of orbits in an integrable system is greatly simplified with the use of angle-action variables (θ, \mathbf{J}) which are canonical coordinates on phase space (e.g. [Binney & Tremaine 2008](#)). By construction, the Hamiltonian $H_0(\mathbf{J})$ does not depend on the angles, so the equations of motion are trivial in these coordinates:

$$\dot{\mathbf{J}} = -\frac{\partial H_0}{\partial \theta} = 0, \quad \dot{\theta} = \frac{\partial H_0}{\partial \mathbf{J}} \equiv \boldsymbol{\Omega}(\mathbf{J}), \quad (5)$$

i.e., the actions are conserved and the conjugate angles increase linearly with time at constant rate $\boldsymbol{\Omega}(\mathbf{J})$.

In a spherically symmetric potential, a convenient set of actions are $\mathbf{J} = (J_r, L, L_z)$ where J_r is the radial action, L is the total angular momentum, and L_z is the z -component of L . The ratio between L and L_z defines the orbital inclination $\beta \equiv \cos^{-1}(L_z/L)$. The conjugate angle variables $\theta = (\theta_r, \theta_\psi, \theta_\varphi)$ describe, respectively, the radial phase, the azimuthal phase in the orbital plane, and the (fixed) longitude of the ascending node, i.e. the intersection of the orbital plane and the galactic equatorial plane.

3 TORQUE IN THE FAST REGIME

To compare our approach (section 4) with the conventional approximations, we here briefly review the torque formula in the fast regime developed by TW84 and W04. Following W04, we solve for the second-order torque using the linear solution to the collisionless

Boltzmann equation. We will demonstrate the breakdown of the formula in the slow regime and discuss the cause of problem. Note that throughout the paper we ignore the halo's self-gravitational perturbation.

We assume that the halo is in a steady state prior to bar formation. The unperturbed distribution is then a function of the actions alone $f_0(\mathbf{J})$ (Jeans' theorem). When the bar forms, the perturbing potential changes the halo's distribution by $f_1(\boldsymbol{\theta}, \mathbf{J}, t)$. We can then write the Hamiltonian H and the distribution function f as

$$H(\boldsymbol{\theta}, \mathbf{J}, t) = H_0(\mathbf{J}) + \Phi_1(\boldsymbol{\theta}, \mathbf{J}, t), \quad f(\boldsymbol{\theta}, \mathbf{J}, t) = f_0(\mathbf{J}) + f_1(\boldsymbol{\theta}, \mathbf{J}, t), \quad (6)$$

where Φ_1 consists of the bar potential (3) and the self-gravitational perturbation induced by the response of the halo f_1 , although here we ignore the latter. The angle variables are by construction 2π periodic, so one can expand the perturbations into a Fourier series:

$$\Phi_1(\boldsymbol{\theta}, \mathbf{J}, t) = \sum_{\mathbf{n}} \hat{\Phi}_{\mathbf{n}}(\mathbf{J}, t) e^{i\mathbf{n} \cdot \boldsymbol{\theta}}, \quad f_1(\boldsymbol{\theta}, \mathbf{J}, t) = \sum_{\mathbf{n}} \hat{f}_{\mathbf{n}}(\mathbf{J}, t) e^{i\mathbf{n} \cdot \boldsymbol{\theta}}, \quad (7)$$

where $\mathbf{n} = (n_r, n_\psi, n_\varphi)$ is a vector of integers. $\hat{\Phi}_{\mathbf{n}}(\mathbf{J}, t)$ is given in Appendix B. The torque exerted on a single orbit is then

$$\frac{dL_z}{dt} = -\frac{\partial H}{\partial \theta_\varphi} = -i \sum_{\mathbf{n}} n_\varphi \hat{\Phi}_{\mathbf{n}}(\mathbf{J}, t) e^{i\mathbf{n} \cdot \boldsymbol{\theta}}, \quad (8)$$

and the total torque integrated over the full distribution is

$$\begin{aligned} \left\langle \frac{dL_z}{dt} \right\rangle &= \int d^3 J d^3 \boldsymbol{\theta} f(\boldsymbol{\theta}, \mathbf{J}, t) \frac{dL_z}{dt} \\ &= \int d^3 J d^3 \boldsymbol{\theta} \left[f_0(\mathbf{J}) + \sum_{\mathbf{n}} \hat{f}_{\mathbf{n}}(\mathbf{J}, t) e^{i\mathbf{n} \cdot \boldsymbol{\theta}} \right] \left[-i \sum_{\mathbf{n}'} n'_\varphi \hat{\Phi}_{\mathbf{n}'}(\mathbf{J}, t) e^{i\mathbf{n}' \cdot \boldsymbol{\theta}} \right]. \end{aligned} \quad (9)$$

The first term vanishes upon integration over $\boldsymbol{\theta}$ and the second term is non-zero only when $\mathbf{n}' = -\mathbf{n}$, so

$$\left\langle \frac{dL_z}{dt} \right\rangle = i (2\pi)^3 \sum_{\mathbf{n}} n_\varphi \int d^3 J \hat{f}_{\mathbf{n}}(\mathbf{J}, t) \hat{\Phi}_{\mathbf{n}}^*(\mathbf{J}, t), \quad (10)$$

where we used $\hat{\Phi}_{-\mathbf{n}} = \hat{\Phi}_{\mathbf{n}}^*$ as required by $\text{Im}[\Phi_1] = 0$. We see from the above equation that the torque is second order in the perturbation. To proceed, we need to develop the response $\hat{f}_{\mathbf{n}}(\mathbf{J}, t)$ as a function of the potential perturbation $\hat{\Phi}_{\mathbf{n}}(\mathbf{J}, t)$. This is described by the collisionless Boltzmann equation (CBE):

$$\frac{df}{dt} = \frac{\partial f}{\partial t} + \frac{\partial f}{\partial \boldsymbol{\theta}} \cdot \frac{\partial H}{\partial \mathbf{J}} - \frac{\partial f}{\partial \mathbf{J}} \cdot \frac{\partial H}{\partial \boldsymbol{\theta}} = 0. \quad (11)$$

Using the Fourier decomposition for both f and H , we have, for each \mathbf{n} ,

$$\begin{aligned} \frac{\partial \hat{f}_{\mathbf{n}}}{\partial t} + i\mathbf{n} \cdot \boldsymbol{\Omega} \hat{f}_{\mathbf{n}} - i\mathbf{n} \cdot \frac{\partial f_0}{\partial \mathbf{J}} \hat{\Phi}_{\mathbf{n}} \\ + \sum_{\mathbf{n}'} \left[i(\mathbf{n} - \mathbf{n}') \cdot \frac{\partial \hat{\Phi}_{\mathbf{n}'}}{\partial \mathbf{J}} \hat{f}_{\mathbf{n}-\mathbf{n}'} - i\mathbf{n}' \cdot \frac{\partial \hat{f}_{\mathbf{n}-\mathbf{n}'}}{\partial \mathbf{J}} \hat{\Phi}_{\mathbf{n}'} \right] = 0. \end{aligned} \quad (12)$$

The standard prescription to solve this for $\hat{f}_{\mathbf{n}}$ is to ignore the non-linear terms inside the square bracket assuming that both $|f_1/f_0|$ and $|\Phi_1/H_0|$ are sufficiently small. This yields the linearized CBE, which has the following solution for an external perturbation imposed after $t = 0$:

$$\hat{f}_{\mathbf{n}}(\mathbf{J}, t) = i\mathbf{n} \cdot \frac{\partial f_0}{\partial \mathbf{J}} \int_0^t dt' e^{-i\mathbf{n} \cdot \boldsymbol{\Omega}(t-t')} \hat{\Phi}_{\mathbf{n}}(\mathbf{J}, t'). \quad (13)$$

Substituting equation (13) to (10) yields the general torque formula

$$\begin{aligned} \left\langle \frac{dL_z}{dt} \right\rangle &= - (2\pi)^3 \sum_{\mathbf{n}} n_\varphi \int d^3 \mathbf{J} \mathbf{n} \cdot \frac{\partial f_0}{\partial \mathbf{J}} \\ &\quad \times \left[\int_0^t dt' e^{-i\mathbf{n} \cdot \boldsymbol{\Omega}(t-t')} \hat{\Phi}_{\mathbf{n}}(\mathbf{J}, t') \right] \hat{\Phi}_{\mathbf{n}}^*(\mathbf{J}, t). \end{aligned} \quad (14)$$

For a perturbation with constant amplitude and pattern speed Ω_p , the time dependence separates as $\hat{\Phi}_{\mathbf{n}}(\mathbf{J}, t) = \hat{\Phi}_{\mathbf{n}}(\mathbf{J}) e^{-i n_\varphi \Omega_p t}$, and we have (W04)

$$\left\langle \frac{dL_z}{dt} \right\rangle = - (2\pi)^3 \sum_{\mathbf{n}} n_\varphi \int d^3 \mathbf{J} \mathbf{n} \cdot \frac{\partial f_0}{\partial \mathbf{J}} |\hat{\Phi}_{\mathbf{n}}(\mathbf{J})|^2 \frac{\sin[(\mathbf{n} \cdot \boldsymbol{\Omega} - n_\varphi \Omega_p) t]}{\mathbf{n} \cdot \boldsymbol{\Omega} - n_\varphi \Omega_p}, \quad (15)$$

which, in the time-asymptotic limit $t \rightarrow \infty$, reduces to the LBK formula (Lynden-Bell & Kalnajs 1972, TW84)

$$\left\langle \frac{dL_z}{dt} \right\rangle = - (2\pi)^3 \sum_{\mathbf{n}} n_\varphi \int d^3 \mathbf{J} \mathbf{n} \cdot \frac{\partial f_0}{\partial \mathbf{J}} |\hat{\Phi}_{\mathbf{n}}(\mathbf{J})|^2 \pi \delta(\mathbf{n} \cdot \boldsymbol{\Omega} - n_\varphi \Omega_p). \quad (16)$$

W04 and more recently Banik & van den Bosch (2021) emphasized the problem of taking the time-asymptotic limit as the age of the galaxy (and yet less that of the perturbation) may not be longer enough than the relevant dynamical time.

It is obvious from equations (15) and (16) that the torque is dominated by contribution from phase space near resonances, i.e. $\mathbf{n} \cdot \boldsymbol{\Omega} - n_\varphi \Omega_p \approx 0$. However, the vicinity of resonances is precisely where the linearized CBE becomes invalid: the linear response (13) grows indefinitely at resonances (Appendix D), and this will soon violate the assumption that the non-linear terms of the CBE (12) are negligible, which is the basis of this formalism. A correct physical description must respect that the orbits near resonances become trapped, a non-linear secular behaviour that cannot be described by linear theory.

To illustrate the problem, we show in Fig. 1 the torque exerted on the halo by a constantly rotating bar. We compare the torque measured from a test particle simulation (black) with linear theory (equation 15, blue) and the LBK approximation (equation 16, dashed green). For the two approximations, we restrict the summation to the indices with $n_r \in [-10, 10]$, $n_\psi \in [-2, 0, 2]$, and $n_\varphi = 2$. Since both the halo density and the perturbing potential decrease towards large radii, the contributions are largely limited to the main resonances with small r , the strongest being the corotation resonance $\mathbf{n} = (0, 2, 2)$. The top panel shows the evolution for the first 1 Gyr which we see a fair agreement between simulation (black) and time-dependent linear theory (blue) as long as t is sufficiently small compared to the libration periods (of order 1–2 Gyr). However, the linear theory qualitatively fails to predict the subsequent long-term evolution shown in the bottom panel: while the torque of linear theory rapidly converges to a non-zero constant value predicted by the LBK formula, the ‘true’ torque fluctuates over a much longer timescale gradually settling down to zero¹. This relaxation process is driven by phase mixing (a collisionless relaxation), which we describe in the next section.

In this experiment, we have kept the bar's pattern speed constant. If the bar decelerates sufficiently fast that the resonances pass over the orbits before they can respond non-linearly, then resonant trapping

¹ We note that this limit depends on the time-dependence of the perturbation. Here the approach to a steady state (zero torque) is the result of the assumed constant bar pattern speed and amplitude.

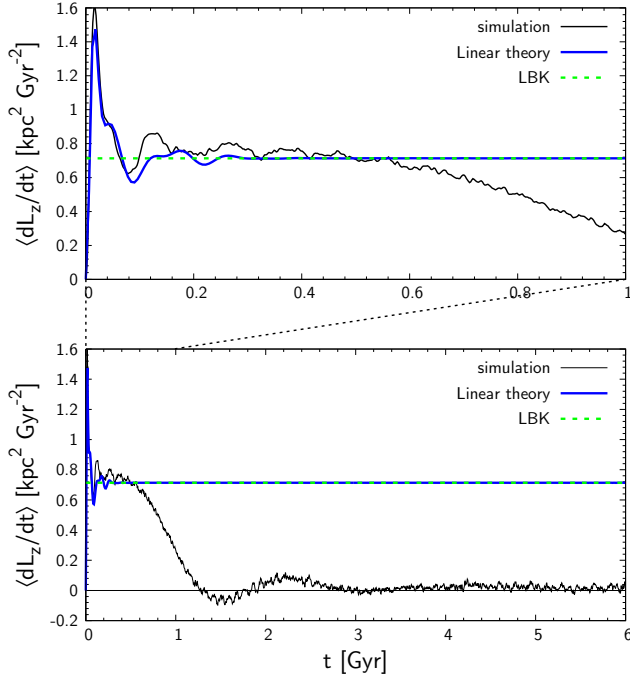


Figure 1. Total torque on the halo (divided by the total halo mass) perturbed by a bar with constant pattern speed and amplitude switched on at $t = 0$. Linear theory (blue, equation 15) agrees with the torque of the test-particle simulation (black) for a few dynamical period (top panel) but fails to predict the long-term evolution (bottom panel). The LBK formula (green, equation 16) gives the time-asymptotic value of linear theory.

will not occur and the formula will predict the right torque for an extended period of time as demonstrated in W04. For this reason, the formula is said to be valid in the *fast regime* (TW84). The validity of the formula is characterized by the speed parameter² (TW84, equation 89):

$$s \equiv \frac{|n_\varphi \dot{\Omega}_p|}{\omega_0^2}, \quad (17)$$

where $\dot{\Omega}_p$ measures the secular evolution of the pattern speed (i.e. not the short-term fluctuations as discussed in Wu et al. 2016) and ω_0 is the libration frequency of trapped orbits at the core of the resonance (equation 25). In the fast regime $s > 1$, orbits cannot stay trapped in resonance because the resonant potential no longer features a local minimum (TW84, Chiba et al. 2021, see also Appendix G).

If the perturbation vanishes before any non-linear effect develops, the formula will be valid regardless of s . This could be the case for e.g. transient spiral arms. Hence, the traditional torque formulas (14)–(16) are appropriate to study the evolution of perturbations that either decelerate rapidly or decay rapidly. Since neither applies to long-lived galactic bars, we must fully model the non-linear response of the halo, i.e. trapping at resonances.

² In the limit of epicycle approximation, the speed parameter reduces to $s \sim \eta/A$ where $\eta \equiv -\dot{\Omega}_p/\Omega_p^2$ is the bar’s dimensionless slowing rate and A the dimensionless bar strength (Chiba et al. 2021, equation 27).

4 TORQUE IN THE SLOW REGIME

4.1 Angle-action variables near resonances

The alternative to solving the non-linear terms in the CBE (12) is to change the coordinates. The majority of orbits near each resonance $N = (N_r, N_\psi, N_\varphi)$ behave quasi-periodically regardless of trapping and thus there exist a new set of angle-action coordinates for them (e.g. TW84; Kaasalainen 1994; Sridhar & Touma 1996; Binney 2016, 2018; Monari et al. 2017). In these ‘true’ angle-action coordinates, the time evolution of the distribution function can be modelled straightforwardly from the non-linearized CBE (section 4.2). In this section, we first lay out the known coordinate transformations, and from there develop our equations for the torque on both trapped and untrapped orbits.

We start with a canonical transformation to the so-called slow-fast angle-action variables $(\theta', J') = (\theta_{f1}, \theta_{f2}, \theta_s, J_{f1}, J_{f2}, J_s)$ (e.g. TW84):

$$\theta_{f1} = \theta_r, \quad \theta_{f2} = \theta_\psi, \quad \theta_s = N \cdot \theta - N_\varphi \Omega_p t, \quad (18)$$

$$J_{f1} = J_r - \frac{N_r}{N_\varphi} L_z, \quad J_{f2} = L - \frac{N_\psi}{N_\varphi} L_z, \quad J_s = \frac{L_z}{N_\varphi}, \quad (19)$$

using the generating function

$$W(\theta, J', t) = \theta_r J_{f1} + \theta_\psi J_{f2} + (N \cdot \theta - N_\varphi \Omega_p t) J_s. \quad (20)$$

The Hamiltonian (6) transforms to

$$H(\theta', J') = H_0(J') - N_\varphi \Omega_p J_s + \sum_k \hat{\Psi}_k(J') e^{ik \cdot \theta'}, \quad (21)$$

where we have expanded the perturbation H_1 into a Fourier series (Appendix B) with indices $\mathbf{k} = (k_{f1}, k_{f2}, k_s)$. The purpose of transforming to the slow-fast variables is to separate the motion into slow and fast components: near the resonance, the slow angle θ_s evolves much slower than the fast angles $\theta_f = (\theta_{f1}, \theta_{f2})$. This allows one to average the Hamiltonian over θ_f while holding θ_s fixed which removes all perturbation terms in (21) with $\mathbf{k}_f = (k_{f1}, k_{f2}) \neq \mathbf{0}$. Since only terms with $k_s = \pm 1$ are non-zero for resonances with $N_\varphi = 2$ (Appendix B), we may write

$$\bar{H}(\theta_s, J') = H_0(J') - N_\varphi \Omega_p J_s + \Psi(J') \cos(\theta_s - \theta_{s,\text{res}}), \quad (22)$$

where $\Psi \equiv 2|\hat{\Psi}_{(0,0,1)}|$. In this averaged system, the two fast actions $J_f = (J_{f1}, J_{f2})$ are conserved, i.e. $\dot{J}_f = -\frac{\partial \bar{H}}{\partial \theta_f} = \mathbf{0}$. Thus this Hamiltonian is integrable: it has three isolating integrals, the two fast actions and the Hamiltonian itself, meaning that angle-action coordinates for \bar{H} exist.

A convenient analytical transformation to the angle-action coordinates of \bar{H} is available if we Taylor expand \bar{H} around the resonance $J_{s,\text{res}}$ up to second order and ignore terms smaller than $|\Psi/H_0|$:

$$\bar{H}(\theta_s, J') \simeq \frac{1}{2} G(J_f, J_{s,\text{res}}) (J_s - J_{s,\text{res}})^2 + \Psi(J_f, J_{s,\text{res}}) \cos(\theta_s - \theta_{s,\text{res}}), \quad (23)$$

where

$$G(J') \equiv \frac{\partial^2 H_0}{\partial J_s^2} = \frac{\partial \Omega_s}{\partial J_s}. \quad (24)$$

The first order derivative of $H_0(J') - N_\varphi \Omega_p J_s$ vanishes at the resonance and we have dropped the constant terms. The approximated Hamiltonian takes the form of a classical pendulum Hamiltonian apart from a different sign. In galactic dynamics, G (equation 24) is in many cases negative (TW84, Figure 5) so in what follows we will

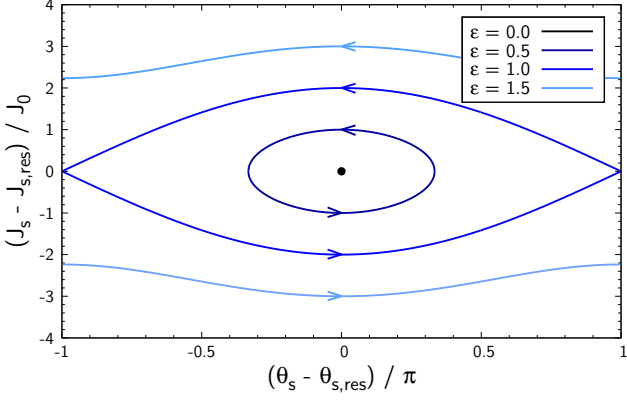


Figure 2. Phase flow for the approximate \bar{H} (23). Level curves of \bar{H} parametrized by ε are plotted. For $0 \leq \varepsilon < 1$, the motion of orbits in θ_s is bounded (libration) whereas for $\varepsilon > 1$, θ_s is unbounded (circulation).

assume $G < 0$ although cases with $G > 0$ can be treated similarly by adjusting $\theta_{s,\text{res}}$ as appropriate. For subsequent use, we define

$$\omega_0^2 \equiv -G\Psi, \quad J_0^2 \equiv -\Psi/G, \quad \varepsilon \equiv \sqrt{\frac{1}{2} \left(1 - \frac{\bar{H}}{\Psi} \right)}. \quad (25)$$

Depending on the value of \bar{H} , parametrized by the dimensionless energy of the pendulum ε , there are two types of qualitatively different motions as depicted in Fig. 2: orbits librate when $0 \leq \varepsilon < 1$ (trapped) and circulate above or below the resonance when $\varepsilon > 1$ (untrapped). $\varepsilon = 1$ defines the separatrix.

In the following, we summarize the canonical transformation from the slow angle-action variables (θ_s, J_s) to the angle-action coordinates of libration/circulation (Brizard 2013), and formulate the secular torque on trapped/untrapped orbits.

4.1.1 Trapped orbits ($0 \leq \varepsilon < 1$)

The angle-action coordinates of libration are

$$\theta_\ell = \theta_{\ell 0} + \Omega_\ell t, \quad \Omega_\ell = \frac{\pi}{2K(\varepsilon)}\omega_0, \quad (26)$$

$$J_\ell = \frac{1}{2\pi} \oint d\theta_s J_s = \frac{8J_0}{\pi} \left[E(\varepsilon) - (1 - \varepsilon^2) K(\varepsilon) \right], \quad (27)$$

where $K(\varepsilon)$ and $E(\varepsilon)$ are the complete elliptic integral of the first and second kinds (Appendix E). ω_0 and J_0 are defined in equation (25). Note that $J_0 > 0$ but $\omega_0 < 0$. The inverse transformation is

$$\theta_s - \theta_{s,\text{res}} = 2 \arcsin \left[\varepsilon \operatorname{sn} \left(\frac{2K(\varepsilon)}{\pi} \theta_\ell \middle| \varepsilon \right) \right], \quad (28)$$

$$J_s - J_{s,\text{res}} = 2J_0 \varepsilon \operatorname{cn} \left(\frac{2K(\varepsilon)}{\pi} \theta_\ell \middle| \varepsilon \right), \quad (29)$$

where sn , cn and dn are the Jacobi elliptic functions (Appendix E). The torque exerted on trapped orbits is then

$$\frac{dL_z}{dt} = N_\varphi \Omega_\ell \frac{dJ_s}{d\theta_\ell} = 2N_\varphi \varepsilon \Psi \operatorname{sn} \left(\frac{2K(\varepsilon)}{\pi} \theta_\ell \middle| \varepsilon \right) \operatorname{dn} \left(\frac{2K(\varepsilon)}{\pi} \theta_\ell \middle| \varepsilon \right), \quad (30)$$

which becomes harmonic near the centre of the resonance:

$$\frac{dL_z}{dt} \simeq 2N_\varphi \varepsilon \Psi \sin \theta_\ell \quad \text{for } \varepsilon \ll 1. \quad (31)$$

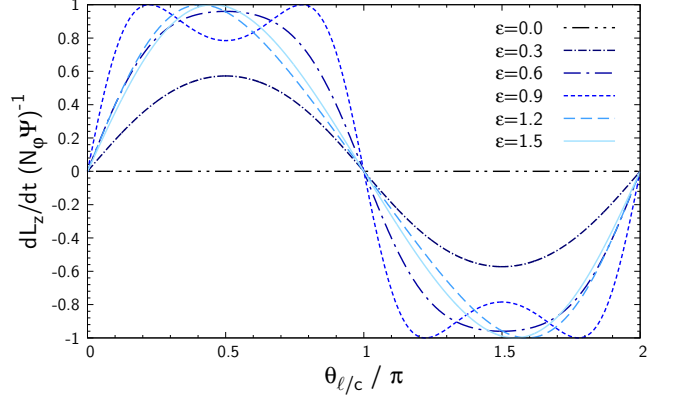


Figure 3. Torque applied to trapped ($\varepsilon < 1$) and untrapped ($\varepsilon > 1$) orbits as a function of the libration/circulation angle $\theta_{\ell/c}$. The behaviour deviates from a sinusoidal wave near the separatrix $\varepsilon = 1$.

4.1.2 Non-trapped orbits ($\varepsilon > 1$)

The angle-action coordinates of circulation are

$$\theta_c = \theta_{c0} + \Omega_c t, \quad \Omega_c = \frac{\pi \varepsilon}{K(\varepsilon^{-1})} \omega_0, \quad (32)$$

$$J_c = \frac{1}{2\pi} \oint d\theta_s J_s = J_{s,\text{res}} \pm \frac{4J_0 \varepsilon}{\pi} E(\varepsilon^{-1}), \quad (33)$$

where the \pm signs correspond to the upper and lower circulating regimes, respectively. Note that the subscript ‘c’ denotes ‘circulating’ (untrapped) orbits and not ‘circular’ orbits. The inverse transformation is

$$\theta_s - \theta_{s,\text{res}} = \pm 2 \arcsin \left[\operatorname{sn} \left(\frac{K(\varepsilon^{-1})}{\pi} \theta_c \middle| \varepsilon^{-1} \right) \right], \quad (34)$$

$$J_s - J_{s,\text{res}} = \pm 2J_0 \varepsilon \operatorname{dn} \left(\frac{K(\varepsilon^{-1})}{\pi} \theta_c \middle| \varepsilon^{-1} \right). \quad (35)$$

In the limit $\varepsilon \rightarrow \infty$, the slow action is conserved and the slow angle θ_s asymptotically approaches the angle of circulation θ_c . The torque exerted on untrapped orbits is

$$\frac{dL_z}{dt} = \pm 2N_\varphi \Psi \operatorname{sn} \left(\frac{K(\varepsilon^{-1})}{\pi} \theta_c \middle| \varepsilon^{-1} \right) \operatorname{cn} \left(\frac{K(\varepsilon^{-1})}{\pi} \theta_c \middle| \varepsilon^{-1} \right). \quad (36)$$

Analogous to (31), far from the resonance, the torque becomes harmonic:

$$\frac{dL_z}{dt} \simeq \pm N_\varphi \Psi \sin \theta_c \quad \text{for } \varepsilon \gg 1. \quad (37)$$

The behaviour of the torque is plotted in Fig. 3. As seen in (31) and (37), the torque fluctuates sinusoidally near the core ($\varepsilon \ll 1$) of the resonance, as well as far from it ($\varepsilon \gg 1$). As predicted from (31), the torque on trapped orbits diminishes towards $\varepsilon = 0$ where it vanishes. Near the separatrix ($\varepsilon \approx 1$), the torque forms a dip at $\theta_\ell = \pi/2, 3\pi/2$ since orbits stagnate near the unstable singular points $(\theta_s - \theta_{s,\text{res}}, J_s - J_{s,\text{res}}) = (\pm\pi, 0)$: in the case of the CR at $J_{f1} = 0$ (circular, $J_r = 0$) and $J_{f2} = 0$ (in-plane, $L = L_z$), these points correspond to the unstable Lagrange points on the bar’s major axis. As the orbit approaches the separatrix, the dip deepens and eventually the torque becomes zero over the entire phase except at $\theta_\ell = 0$ and π . This situation is analogous to a real pendulum in transition from oscillation to circulation that spends most of its time/phase stagnating at the top of the pivot with hardly any change in momentum.

4.2 Evolution of the distribution function

The averaged Hamiltonian \bar{H} (23) now only depends on the new actions $\mathbf{J}'' = (J_{f_1}, J_{f_2}, J_{\ell/c})$ that are conjugate to the new angles $\boldsymbol{\theta}'' = (\theta_{f_1}, \theta_{f_2}, \theta_{\ell/c})$ where the subscript ‘ ℓ/c ’ indicates libration or circulation depending on ε . The collisionless Boltzmann equation (11) for the averaged system is then

$$\frac{\partial f}{\partial t} + \boldsymbol{\Omega}'' \cdot \frac{\partial f}{\partial \boldsymbol{\theta}''} = 0, \quad \text{where} \quad \boldsymbol{\Omega}''(\mathbf{J}'') \equiv \frac{\partial \bar{H}}{\partial \mathbf{J}''}. \quad (38)$$

This equation has the trivial solution

$$f(\boldsymbol{\theta}'', \mathbf{J}'', t) = f(\boldsymbol{\theta}'' - \boldsymbol{\Omega}'' t, \mathbf{J}'', 0). \quad (39)$$

One can thus readily obtain the phase space density at any time $t = \tau$ from the original distribution at $t = 0$ by simply winding the angles backward by τ . Since the initial distribution of the halo (A1) is uniform in the fast angles ($\theta_{f_1}, \theta_{f_2}$) but *not* in the libration/circulation angle $\theta_{\ell/c}$, the system is out of equilibrium after the emergence of the bar and starts phase mixing in $\theta_{\ell/c}$.

Figure 4 shows the evolution of the phase-space density near the corotation resonance (CR) at $(J_{f_1}, J_{f_2}) = (10, 0) \text{ kpc}^2 \text{ Gyr}^{-1}$ plotted every 1 Gyr from top to bottom. The bar is instantaneously switched on at $t = 0$. The left-hand column shows the distribution of the test-particle simulation which is well reproduced by the analytical distribution shown on the right. Inside the separatrix (black curves), the density, initially uniform in the slow angle, phase mixes in the libration angle. Since the libration period increases towards the separatrix, the phase space differentially rotates resulting in a phase-space spiral. Similarly, the phase space outside the separatrix winds into stripes since the circulation period is also maximal (infinite) at the separatrix and drops away from there.

The development of phase-space spiral inside the resonance does not hinge on the instantaneous emergence of the bar. It also happens in a slowly growing bar, as shown in Fig. 5, which displays the same phenomenon for a bar that slowly grows over 4 Gyr following a polynomial prescription (Dehnen 2000, equation 4). Far outside the separatrix, the change is generally adiabatic since the circulation periods are small compared to the timescale on which the potential changes. Here, the circulation action J_c is conserved (see Appendix C) and so the distribution in the circulation angle is kept uniform as it was at $t = 0$, thus showing no stripes. However, the situation is qualitatively different in the trapped region. The separatrix simultaneously engulfs the high-density region from below and the low-density region from above, thus rendering the distribution in the libration angle inevitably nonuniform (almost like a rectangular wave distribution). Due to this abrupt transition between maximum and minimum density, the phase-space spiral in a growing bar has a hard boundary compared to the non-growing case (Fig. 4) which shows a smoother transition between peaks and troughs.

The conservation of J_c also implies that the untrapped orbits bend around the advancing separatrix, i.e. near the midpoint $\theta_s - \theta_{s,\text{res}} = 0$ they bend away from the resonance line and near $\theta_s - \theta_{s,\text{res}} = \pm\pi$ they bend towards the resonance. In the end (Fig. 5, bottom panel), the orbits just above and below the separatrix originate from around $J_s - J_{s,\text{res}} \approx \pm 120 \text{ kpc}^2 \text{ Gyr}^{-1}$, respectively, which leads to the discontinuous step in density at the resonance line when moving along J_s at $\theta_s - \theta_{s,\text{res}} = \pm\pi$.

It is instructive to relate the behaviour in the slow angle-action plane with the Chandrasekhar’s classical picture of dynamical friction, i.e. as an over-density lagging behind the moving object (bar). At the CR, the slow angle (18) is $\theta_s = 2[\theta_\psi - (\varphi_b - \theta_\varphi)]$ where θ_ψ is the azimuthal angle of the guiding orbit in its orbital plane, and $\varphi_b - \theta_\varphi$ is the azimuthal angle of the bar in the galactic plane measured from

the ascending node. The centre of oscillation of the CR is at the bar’s minor axis $\theta_\psi - (\varphi_b - \theta_\varphi) = \pi/2$, so $\theta_{s,\text{res}} = \pi$, and thus the range $\theta_s - \theta_{s,\text{res}} \in [-\pi, \pi]$ corresponds to $\theta_\psi - (\varphi_b - \theta_\varphi) \in [0, \pi]$. Figure 6 shows typical in-plane ($\beta = 0$) orbits in the bar’s corotating frame. For $\theta_s - \theta_{s,\text{res}} > 0$, the trapped orbits are lagging behind the bar, so they exert a negative torque on the bar, while for $\theta_s - \theta_{s,\text{res}} < 0$, they are ahead of the bar, exerting a positive torque on the bar. The net torque is then determined by the distribution in θ_s : In the beginning, the overdensity at small z -angular momentum (or J_s) librates towards $\theta_s - \theta_{s,\text{res}} > 0$ thus giving rise to a net negative torque on the bar. Subsequently, this overdensity librates back and forth between $\theta_s - \theta_{s,\text{res}} > 0$ and $\theta_s - \theta_{s,\text{res}} < 0$, providing a systematic oscillation of dynamical friction, which will fade with phase mixing. Eventually, the distribution in θ_s approaches equilibrium and the net torque on a constantly rotating bar converges to zero as we saw in Fig. 1.

If the external perturbation is transient (e.g. short-lived spiral arms), once the perturbation fades away, the slow angle will recover its role as a true angle variable and thus the halo will resume phase mixing in θ_s . However, since the libration angle θ_ℓ at which the orbits got captured and were released are generally different, the final DF near resonances will be flatter than the original distribution. This ‘scar’ in the DF will affect the evolution of the renewed spiral arms (Sellwood & Carlberg 2014; Sridhar 2019), and can cause self-gravitational instabilities, exciting further spiral modes (Sellwood & Carlberg 2019).

4.3 Onset of chaos by overlap of resonances

By averaging over the fast motions, we have approximated the Hamiltonian near a resonance with an integrable Hamiltonian \bar{H} (23). We now ask whether the system remains integrable when the neglected terms of the full Hamiltonian $\delta H = H - \bar{H}$ are added back in. To consider the effect of δH , we Fourier expand it in the new angles

$$\delta H(\boldsymbol{\theta}'', \mathbf{J}'') = \sum_{\mathbf{m}} \hat{\Psi}_{\mathbf{m}}(\mathbf{J}'') e^{i\mathbf{m} \cdot \boldsymbol{\theta}''}. \quad (40)$$

The Kolmogorov–Arnold–Moser (KAM) theorem (Arnol’d 1963) implies that these terms will only slightly perturb the motion and the system will stay integrable so long as they are small and sufficiently far from satisfying a resonance condition $\mathbf{m} \cdot \boldsymbol{\Omega}'' = 0$ where $\boldsymbol{\Omega}'' = (\Omega_{f_1}, \Omega_{f_2}, \Omega_{\ell/c})$. However, if δH contains a resonant term, it may render the system non-integrable. These *secondary resonances* form new resonant islands (either inside or outside the original separatrix) and can in principle be modelled in much the same way as we have dealt with the original resonance of the unperturbed system H_0 (e.g. Lichtenberg & Lieberman 1992; Malhotra 1998; Wisdom 2004). However, when the separatrices of the secondary resonances come sufficiently close to the separatrix of the original resonances, orbits may behave stochastically, moving from one domain of resonance to another (Chirikov 1979). A significant secondary resonance is expected when two resonances of the unperturbed Hamiltonian H_0 reside close to each other³. The resonances in a bar-halo system indeed overlap at particular regions of phase space and some orbits there turn chaotic/irregular.

To illustrate the overlapping of resonances, we show in Fig. 7 the configuration of bar resonances with $N_\varphi = 2$ and $N_\psi = 2, 0, -2$

³ Outside the original separatrix, the circulation frequency approximates the slow frequency and thus the resonance condition $\mathbf{m} \cdot \boldsymbol{\Omega}'' = 0$ in the resonant system $\bar{H}(\mathbf{J}'')$ approximates the original resonance condition $\mathbf{n} \cdot \boldsymbol{\Omega} - n_\varphi \Omega_p = 0$ in the unperturbed system $H_0(\mathbf{J})$.

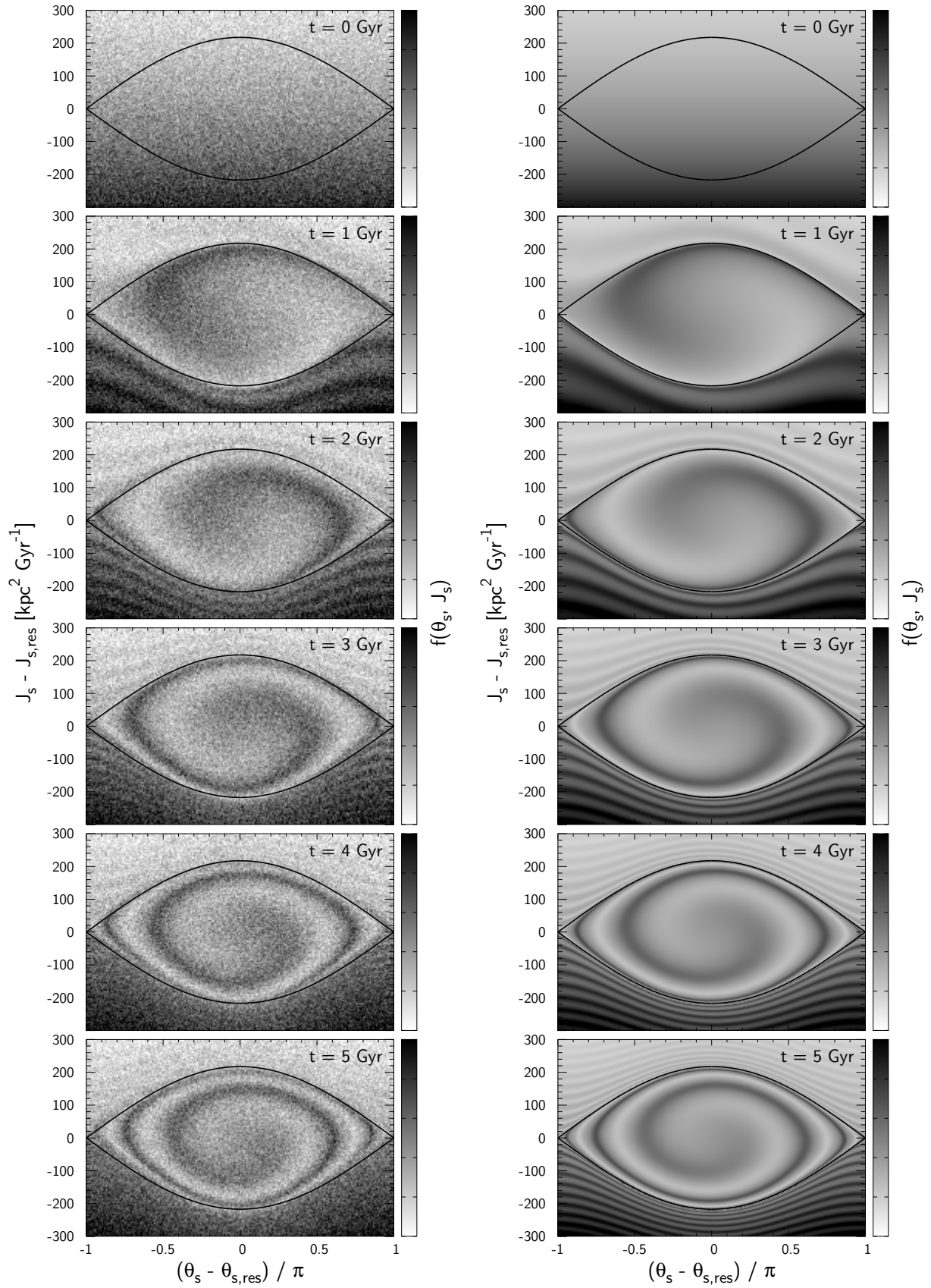


Figure 4. Time evolution of the phase-space density $f(\theta_s, J_s)$ near the corotation resonance $N = (0, 2, 2)$ at $(J_{f_1}, J_{f_2}) = (10, 0) \text{ kpc}^2 \text{ Gyr}^{-1}$ plotted every 1 Gyr. Left column: test particle simulation. Right column: analytical (equation 39). Black curves mark the separatrix.

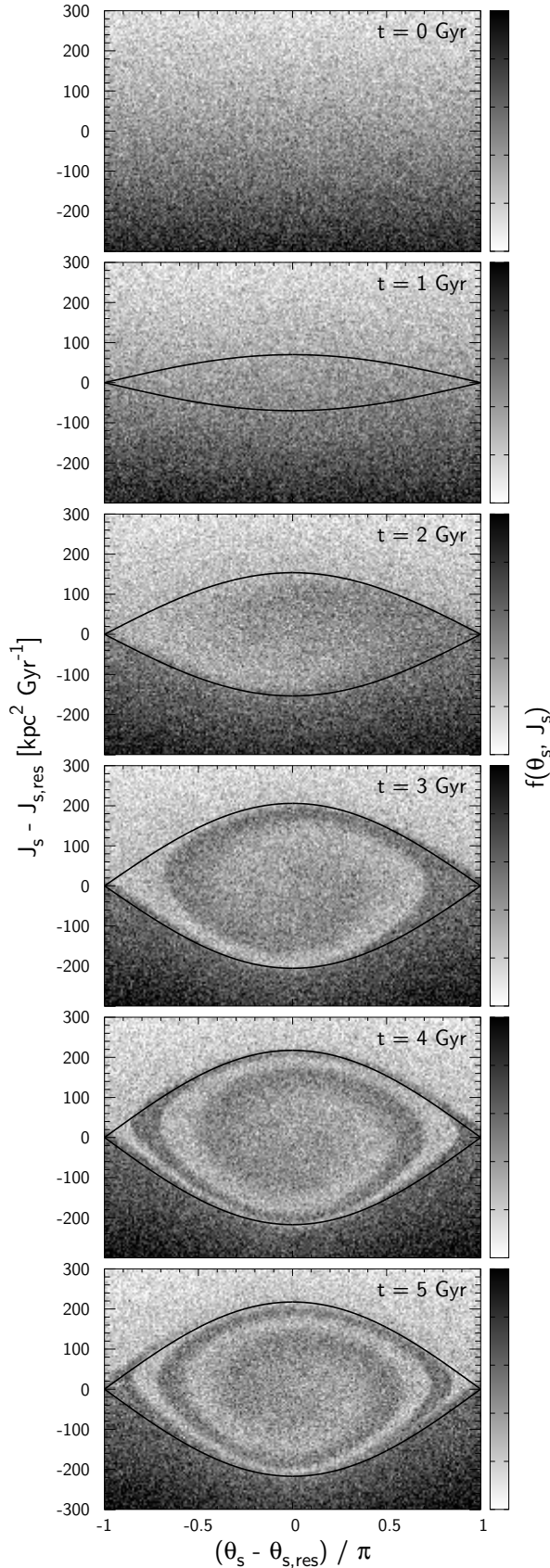


Figure 5. Phase-space density of the halo perturbed by a bar growing slowly in 4 Gyr. The distribution outside the resonance is smooth due to the adiabatic emergence of the bar, while that inside the resonance displays a winding spiral since the expanding separatrix simultaneously captures orbits from above (low density) and below (high density).

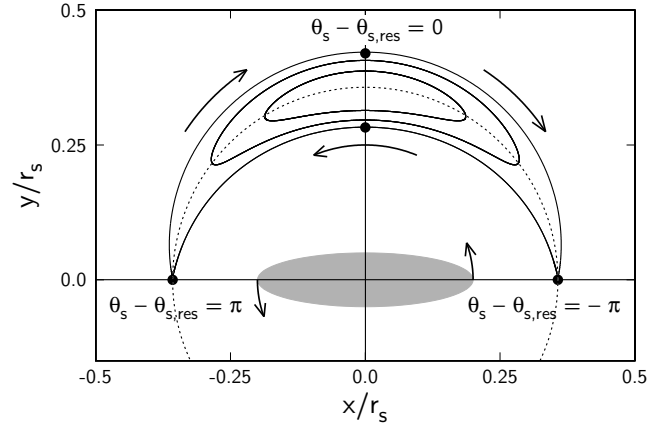


Figure 6. Guiding orbits of particles in the galactic plane ($\beta = 0$) trapped in the CR of the bar (gray ellipse). Resonantly trapped orbits at $\theta_s - \theta_{s,res} > 0$ ($x < 0$) are pulled forward by the bar (gain angular momentum), while those at $\theta_s - \theta_{s,res} < 0$ ($x > 0$) are pulled back by the bar (lose angular momentum). The net torque on the bar is determined by the phase distribution of these trapped dark matter. As they slowly phase mix, the net torque attenuates.

from top to bottom. A figure overlaying the three resonances is given in Appendix F. In a spherical system, the resonant condition only depends on L and J_r . However, the volume of the trapped zone depends in addition on the orbital inclination $\beta \equiv \cos^{-1}(L_z/L)$. We thus show three plots from left to right with $\beta = 0$ (prograde), $\beta = \pi/2$ (perpendicular), and $\beta = \pi$ (retrograde). Following Binney (2018), we draw the furthest excursions of trapped orbits with dotted curves and mark the direction of libration with thin black lines. The colors show the phase-space density of the unperturbed distribution function (A1).

The top panels of Fig. 7 show resonances with $N_\psi = 2$ which are familiar in disc dynamics: the resonance at the bottom-left corner is the corotation resonance (CR, $N_r = 0$) and the neighboring one is the outer Lindblad resonance (OLR, $N_r = 1$). In our model, resonances with negative N_r including the inner Lindblad resonance (ILR, $N_r = -1$) have negligibly small volume⁴. The trapped volume is largest at $\beta = 0$ (left, in-plane prograde), and decreases towards $\beta = \pi$ (right, in-plane retrograde) where it vanishes. The panels in the middle row present resonances with $N_\psi = 0$. Orbits trapped in these resonances complete N_ψ radial oscillations in N_r bar period regardless of their azimuthal phase with respect to the bar. Weinberg & Katz (2007) called these resonances the *direct radial resonances* (DRRs). The strength/size of DRRs peaks at $\beta = \pi/2$. The lowest panels show resonances with $N_\psi = -2$ which are strongest at $\beta = \pi$.

Comparing the different sets of resonances, we can see from Fig. 7 that the resonances partly overlap especially near $\beta \approx \pi/2$, where all resonances fill a finite phase-space volume (see Fig. F1 for a directly superimposed plot). To see the impact of resonance overlap, we plot in Fig. 8 four orbits trapped in the OLR $N = (1, 2, 2)$ with different initial actions marked by black points in Fig. 7. As expected, the two orbits at $\beta = 0$ (circle and rhombus, left column in Fig. 8) are well modelled by the averaged Hamiltonian (blue), since only resonances with $N_\psi = 2$ has a non-zero volume. The right-hand column of Fig. 8

⁴ This contrasts with the models of W04 which are dominated by the ILR. The discrepancy is most likely due to the difference in the adopted bar pattern speed: our pattern speed $\Omega_p \approx 35.8$ Gyr corresponds to $R_{ILR} \sim 0.25$ kpc in our Hernquist halo, whereas their initial Ω_p is much lower which implies larger R_{ILR} and thus more mass trapped in the ILR.

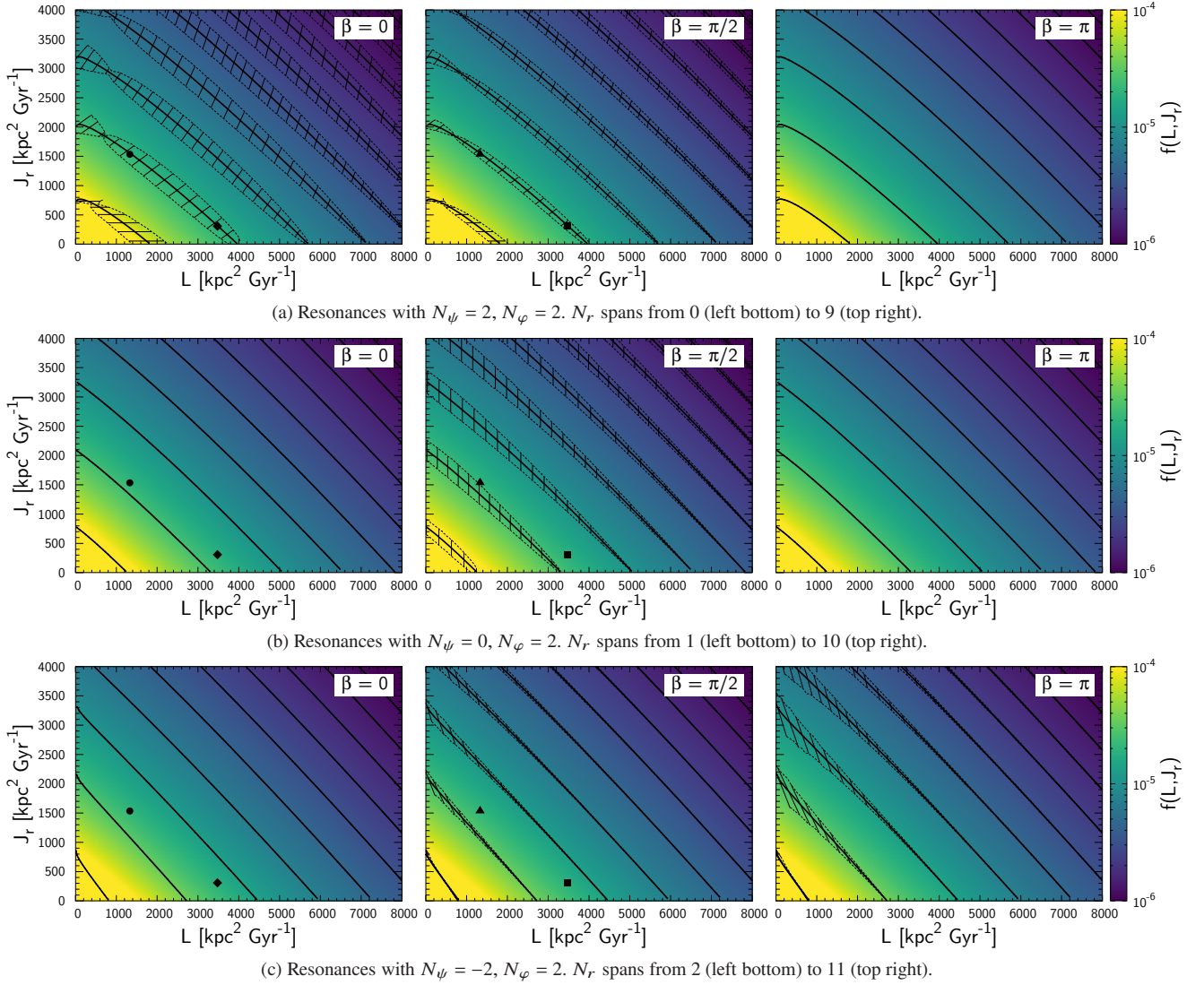


Figure 7. Bar-halo resonances $N = (N_r, N_\psi, N_\phi)$ at three different orbital planes $\beta = \cos^{-1}(L_z/L) = 0, \pi/2, \pi$ from left to right. The thick black curves mark the location of resonances, the dotted curves mark the maximum extent of the separatrix, and the thin black lines mark the direction of libration. The colors show the phase-space density in log scale. Top panel: Resonances with $N_\psi = 2$. Resonantly trapped volume is largest at $\beta = 0$ and vanishes at $\beta = \pi$. The black symbols, placed on the outer Lindblad resonance $N = (1, 2, 2)$, mark the initial actions of orbits shown in Fig. 8. Middle panel: Resonances with $N_\psi = 0$. Trapped volume is largest at $\beta = \pi/2$ and decays towards $\beta = 0, \pi$. Bottom panel: Resonances with $N_\psi = -2$. Trapped volume increase towards $\beta = \pi$.

(triangle and square) shows two contrasting examples for $\beta = \pi/2$: the bottom right orbit (square) is mildly distorted as it is near, but still outside the second resonance, while the top right orbit (triangle) shows marked excursions as it is within the region of the $N = (2, 0, 2)$ resonance. We note that we ascribe only the large-scale distortions to the presence of the second resonance, e.g. the irregular dip near $\theta_s - \theta_{\text{res}} \approx 0$. The step-like behaviour seen in the figure comes from the high eccentricity of the orbit (large J_r and small L), i.e. the fast change in L_z when an orbit rapidly passes near the bar at its pericentre.

When the domains of two resonances overlap, orbits may also pass from one resonance to another. Figure 9 shows an example of such an orbit moving between the OLR and the $(2, 0, 2)$ resonance. When viewed in the slow plane of the OLR (left panel), the orbit is initially trapped and then escapes the resonance after roughly one cycle of libration. In contrast, from the viewpoint of the $(2, 0, 2)$

resonance (right panel), the orbit is at first outside the resonance but then becomes trapped soon after it left the OLR at around 9 Gyr.

The important question here is how much does the overlap of resonances affect the calculation of the net torque based on the averaged Hamiltonian? The first thing to mention is that the three sets of resonances with $N_\psi \in 2, 0, -2$ have their main territories at $\beta = 0, \pi/2, \pi$ respectively, so the majority of resonant phase-space is well isolated. Secondly, the irregular/chaotic orbits found at the overlapped regions still librate quasi-periodically around one of the two resonances over a finite time interval. Thirdly, these oscillations on top of the libration behave mostly stochastically without any apparent law, so it should not leave a systematic bias when averaged over the whole set of orbits. Hence we do not expect significant loss of accuracy in estimating the torque using the averaged Hamiltonian. We will demonstrate this below with test particle simulations.

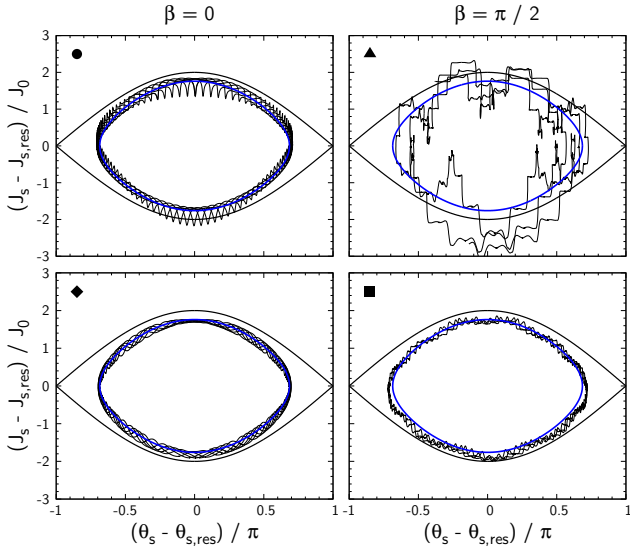


Figure 8. Motion of orbits trapped at the OLR. The symbol on the left top corner represent the position of the initial actions marked in Fig. 7. The black orbits are integrated numerically using the full Hamiltonian and the blue orbits are obtained analytically from the averaged Hamiltonian. The orbit at the top-right panel exhibits chaotic oscillations as it is overlapped by the $N = (2, 0, 2)$ resonance. All orbits take similar values of $\varepsilon \sim 0.9$.

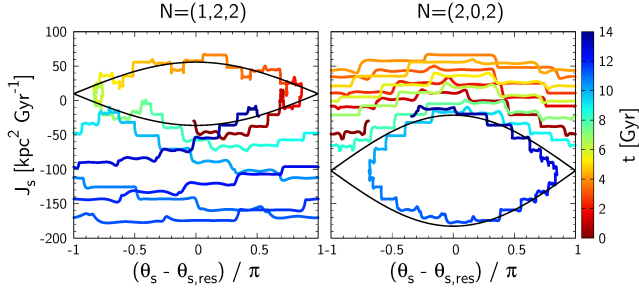


Figure 9. Both panels show the same orbit in the angle-action plane of the $N = (1, 2, 2)$ (OLR, left-hand) and the $N = (2, 0, 2)$ resonance (right-hand). Colours encode the time. The orbit is initially on the OLR and then passes to the $N = (2, 0, 2)$ resonance.

4.4 Total torque on the halo

After these preliminary considerations, we can now achieve our goal to estimate the torque between the bar and the dark halo. Using equation (30), (36), and (39), we obtain the total torque by summation over all resonances N :

$$\begin{aligned} \left\langle \frac{dL_z}{dt} \right\rangle &= \sum_N \int d^3 J'' d^3 \theta'' f(\theta'', J'', t) \frac{dL_z}{dt} \\ &= 8(2\pi)^2 \sum_N N_\varphi \int d^2 J_f \Psi J_0 \\ &\times \left[\int_0^1 d\varepsilon \varepsilon^2 \hat{K} \int_0^{2\pi} d\theta_\ell f(\theta_\ell - \Omega_\ell t, J'', 0) \operatorname{sn}(\hat{K}\theta_\ell | \varepsilon) \operatorname{dn}(\hat{K}\theta_\ell | \varepsilon) \right. \\ &\left. \pm \int_1^{\varepsilon_{\text{cut}}} d\varepsilon \tilde{K} \int_0^{2\pi} d\theta_c f(\theta_c - \Omega_c t, J'', 0) \operatorname{sn}(\tilde{K}\theta_c | \varepsilon^{-1}) \operatorname{cn}(\tilde{K}\theta_c | \varepsilon^{-1}) \right], \end{aligned} \quad (41)$$

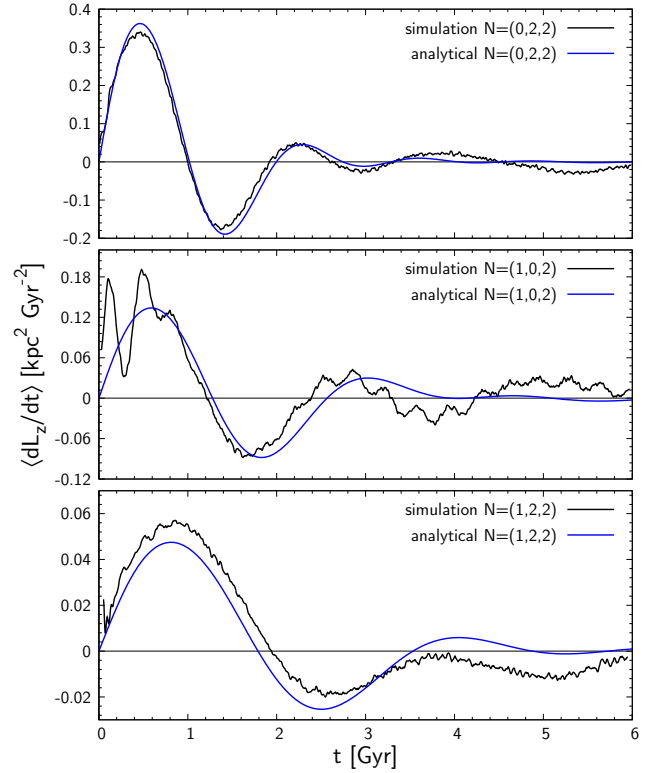


Figure 10. Total torque on orbits trapped in each resonance divided by the total halo mass. From top to bottom, the three strongest resonances are shown (note the different y-axis scale in each figure). The analytical curves (blue) agree well with that of the simulation (black).

where f is the distribution function (39) dependent on the libration/circulation angle $\theta_{\ell/c}$ and the resonant actions $J'' = (J_{f1}, J_{f2}, J_{\ell/c})$, Ψ is the bar perturbation (B9), J_0 measures the width of the resonance (25), and ε parametrizes the value of the Hamiltonian \tilde{H} (25). sn , cn and dn are the Jacobi's elliptic functions (E5-E7) and we have defined $\hat{K} \equiv 2K(\varepsilon)/\pi$ and $\tilde{K} \equiv K(\varepsilon^{-1})/\pi$ where K is the complete elliptic integral of the first kind (E1). The first term in the square bracket describes the torque applied on the trapped phase-space while the second term describes the torque on the untrapped phase-space which we cut at $\varepsilon_{\text{cut}} (> 1)$ to avoid duplicately integrating the phase space between neighbouring resonances. However duplication cannot be fully avoided where resonances overlap. As described above and demonstrated below, we expect the effects of overlapping to be minor and defer detailed modelling for the overlap regions to future study. Here, we cut the integration universally at $\varepsilon_{\text{cut}} = 2 - 3$ which is roughly the ratio of the width and interval between the neighbouring resonances (Fig. 7). The \pm sign in (41) denotes integration over the upper and the lower circulating regions for which the mapping from (θ_c, J'') to $J = (J_r, L, L_z)$ is different.

Figure 10 compares the net torque on trapped orbits calculated with the analytical approach (blue) to a test-particle simulation (black). From top to bottom, we show the torques on the three strongest resonances: $(N_r, N_\psi, N_\varphi) = (0, 2, 2)$, $(1, 0, 2)$, and $(1, 2, 2)$. We select the trapped orbits in the test-particle simulation by demanding that they never pass $\theta_s - \theta_{s,\text{res}} = \pm\pi$. We then place the particles back to their initial coordinates, re-run the simulation exclusively for these particles, and sum up their torque. For all three resonances, the analytical torque (blue) captures the principal features of the

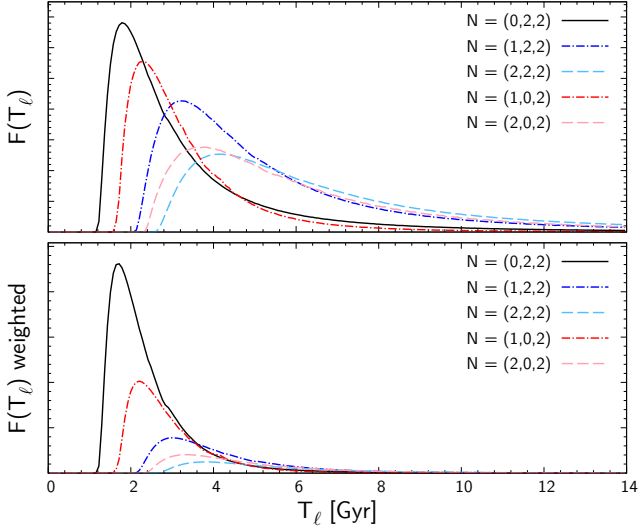


Figure 11. Top panel: Distribution of trapped orbits in libration period. Bottom panel: Distribution weighted by the amplitude of the torque, which provides the actual spectrum of the total torques shown in Fig. 10.

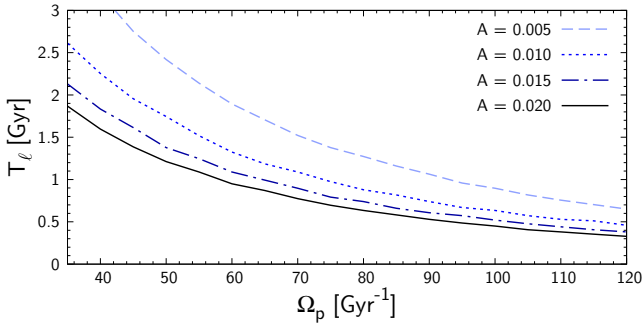


Figure 12. The libration period of the CR at the peak of its distribution $F(T_\ell)$ vs. bar pattern speed Ω_p and bar strength A .

simulation (black), i.e. the torque fluctuates and damps as phase progresses inside each resonance.

To better quantify the time dependence of the torque, we plot the spectra of libration periods in the top panel of Fig. 11. The distribution of each resonance peaks at a period which matches the main oscillating period of the total torque shown in Fig. 10. Since the majority of orbits with long libration periods are those trapped at small Ψ (rather than those near the separatrix) and thus have little impact on the total torque, we plot on the lower panel of Fig. 11 the distribution when weighted by the amplitude of the torque on each orbit. Note though that this is not a Fourier analysis of Fig. 10 since the torque on individual orbits becomes increasingly non-sinusoidal when approaching the separatrix (Fig. 3). The weighted distribution clarifies that the dominant contribution to the torque comes from the corotation resonance and in particular from those with libration period ~ 2 Gyr.

The libration period depends on both the bar pattern speed and the bar strength which vary over time. A simple scaling suggests $T_\ell \sim \omega_0^{-1} = |G\Psi|^{-1/2} \sim \Omega_p^{-1} A^{-1/2}$. Figure 12 shows the mode of the distribution of libration period for a given pattern speed Ω_p and bar strength A . As expected, the libration period is shorter for higher pattern speed and for stronger bars. Since the bar directly

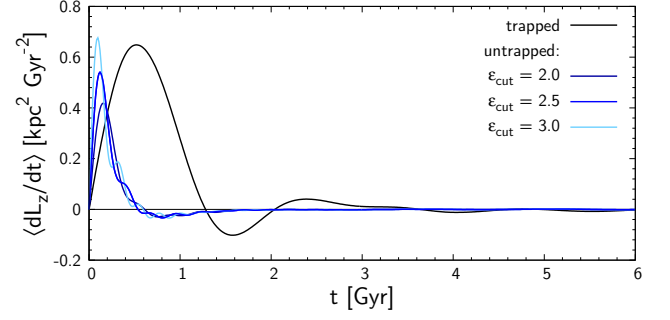


Figure 13. Comparison between the total torque exerted on resonantly trapped (black) and untrapped (blue) orbits in the dark halo. We cut the integration over the untrapped phase space at ϵ_{cut} to avoid duplication by neighbouring resonances. Dynamical friction by trapped and untrapped orbits rises and decays over different timescales.

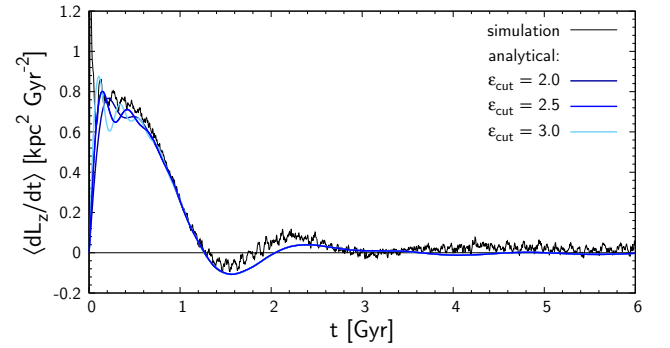


Figure 14. Total torque on the dark halo. The theoretical curve (blue, equation 41) quantitatively explains the behaviour of the simulation (black).

after formation is expected to be faster and weaker than at present, the initial torque (and thus the initial pattern speed) in an expected parameter range typical for the Milky Way should have fluctuated with roughly a Gyr period.

Figure 13 compares the contribution to the total torque from trapped and untrapped phase space with three cutoff $\epsilon_{\text{cut}} = \{2, 2.5, 3\}$. As before, we summed over the resonances with $N_r \in [-10, 10]$, $N_\psi \in [-2, 0, 2]$, and $N_\phi = 2$. The torques on trapped and untrapped orbits rise and decay on different timescales which simply reflects the difference in their orbital periods, i.e. the period of circulation is generally shorter than that of libration. As we increase the upper limit of integration ϵ_{cut} , the total torque on untrapped orbits gets larger and slightly shifts towards early time because contributions from orbits with short circulation periods far away from the resonances are added into the calculation.

Figure 14 shows the sum of trapped and untrapped components (blue) which quantitatively reproduces the total torque of the simulation (black). The result assures us that the trapped orbits comprise the majority of the torque at late times. In the very early times < 0.1 Gyr, the torque of the simulation rises sharply as high as $1.6 \text{ kpc}^2 \text{ Gyr}^{-2}$ (see Fig. 1 for the full range) but our model fails to predict this rapid response for several reasons: (i) we have neglected the fast non-resonant terms of the perturbation by averaging over the fast angles, (ii) the second order Taylor approximation makes our model inaccurate in the region of rapid circulation far from the resonances, (iii) there is a substantial volume of untrapped phase-space that were not integrated due to the cutoff at ϵ_{cut} .

5 SLOWDOWN OF THE BAR

The natural progression of this work will be a self-consistent model for the slowdown/growth of the bar. However, the bar's moment of inertia is not a constant, the halo's self-gravity will amplify the torque, and the inflow of gas towards the nuclear disc provides an additional angular momentum term. Resolving these issues is beyond the scope of this paper, and so must be deferred to future analysis. Instead, here we will discuss the effects of bar slowdown on the angular momentum balance using the bar's slowing rate directly measured from local stellar kinematics (Chiba et al. 2021) which agrees with N -body+smooth particle hydrodynamics simulation of the bar in a live dark halo (Aumer & Schönrich 2015).

Figure 15 shows the phase space perturbed by a bar that slows with $\Omega_p \propto 1/t$ from an initial value $\Omega_{p0} = 81.8 \text{ Gyr}^{-1}$ with rate $\eta \equiv -\dot{\Omega}_p/\Omega_p^2 = 0.004^5$. The bar strength is fixed to $A = 0.02$. As the bar slows, the resonantly trapped orbits get dragged with the resonance towards larger J_s while they keep phase mixing internally. The dot-dashed curves show the separatrix evaluated in a 'time-frozen' Hamiltonian (when fixing the pattern speed) while the solid curves mark the approximate boundary of orbits that remain trapped in the moving resonance (Appendix G). As described in Chiba et al. (2021), the deceleration tilts the potential of the resonance (G6), making the effective trapped region shrink and shift towards positive θ_s , which could also be ascribed to the Euler force arising from the deceleration of the rotating frame of reference.

5.1 Capture and escape from resonance

Resonance sweeping leaves a significant change in the distribution through capture and loss. When the resonance sweeps outwards, the untrapped orbits swept over by the upper separatrix (dot-dashed curves in Fig. 15) will temporarily get trapped, as adiabaticity is broken near the separatrix. Orbits that crossed the upper separatrix near $\theta_s - \theta_{\text{res}} = \pi$ may reach the adiabatic region (solid curves), where the libration action is conserved, and thus remain trapped and get dragged by the resonance. Other orbits will escape the resonance before completing one cycle of libration, proceeding to the lower circulating zone. Depending on the angle θ_s at which these uncaptured orbits enter the resonance, they will travel a different amount of distance in J_s : orbits crossing the separatrix near $\theta_s - \theta_{\text{res}} = -\pi$ will immediately escape the resonance, ending up at a relatively low J_s , while those that could almost but not quite reach the adiabatic region will be dragged a large distance in J_s before they get damped out of the resonance. Thus, after the passage of the resonance, orbits originally at the same action J_{s0} (same color in the right column of Fig. 15) will spread over a wide range of J_s . These orbits then phase mix and form phase-space stripes in the lower circulating region.

As seen in Fig. 15, the entire trapped volume (and the adiabatic region within) generally grows as the bar slows. Inside the adiabatic region, trapped orbits conserve their libration action J_ℓ , so the newly captured orbits accrete on the surface of the adiabatic region. As a result, the resonance grows like a tree ring, where the J_s of origin increases from the core towards the surface (Chiba & Schönrich 2021).

Previous studies formalized the capturing and escaping processes

in the adiabatic limit ($s \ll 1$) by the transition probability averaged over the libration/circulation angles $\theta_{\ell/c}$ (e.g. Henrard 1982; Sridhar & Touma 1996; Collett et al. 1997). However, the angle-averaged probability has little use in modelling dynamical friction since it assumes uniform distribution in $\theta_{\ell/c}$. To model the transient behaviour of dynamical friction, a phase dependent prescriptions for the capture/loss is required. A straightforward way would be to numerically integrate the equations of motion of the averaged Hamiltonian with time-dependent pattern speed (Weinberg & Katz 2007). Alternatively, one could return to the Eulerian approach (section 3) and fully address the non-linear terms of the CBE. This approach can in principle model the resonant structure with arbitrary time-dependence (e.g. bar growth), although it has the difficulty that increasing numbers of higher order modes will be required to model the fine structures developed by phase mixing.

5.2 Transfer of angular momentum by resonant dragging

In addition to the torque caused by phase mixing, the moving resonances give rise to another type of angular momentum transfer. The conservation of libration action ensures that the adiabatic region preserves the phase-space density at the time of capture. Since the resonances move towards higher angular momentum, this implies that the population on resonances is much denser than the surrounding phase space. When resonances move outward, the freed phase space below them will be filled with orbits jumping across the resonances, and just like lifting a heavy body in water, the halo gains net angular momentum which further slows the bar (i.e. positive feedback).

If we accelerate the bar instead, the resonances sweep inwards. As long as they are still denser than the surrounding phase space, the resonance frees angular momentum, further accelerating the bar (i.e. again, positive feedback). However, as the resonances proceed deep into the inner halo, the surrounding density rises and so the amount of freed angular momentum decreases up to even becoming negative when the resonances are underdense (i.e. negative feedback).

TW84 and Weinberg (1985) called these types of angular momentum exchange the 'dynamical feedback' and presented a formula to predict its amount in the slow (adiabatic) limit although they only figured in the change in angular momentum due to orbits that jump across the resonance and separately discussed the effect of resonant dragging. They gave an insightful interpretation of dynamical feedback as a change in moment of inertia of the bar: since dynamical feedback is to first order proportional to the change in pattern speed, ($\tau_{\text{feedback}} = C\dot{\Omega}_p$, where $C > 0$), the equation of motion for the bar becomes (Weinberg 1985)

$$\dot{\Omega}_p = \frac{\tau_{\text{friction}} + \tau_{\text{feedback}}}{I_b} = \frac{\tau_{\text{friction}}}{I_b - C} \quad (42)$$

where the term τ_{friction} represents dynamical friction and I_b is the bar's moment of inertia. This equation implies that dynamical feedback translates as a reduction in the moment of inertia. However we caution that (i) the equation is only valid in the slow limit where the orbits adiabatically respond to the change in pattern speed. The response at resonances is always delayed by an order of the libration period, meaning that for a rapidly fluctuating torque caused by e.g. the bar-spiral interactions, the bar will react with its bared moment of inertia. (ii) C is not a constant and depends both on the pattern speed Ω_p as well as its derivative $\dot{\Omega}_p$. In particular, C is a decreasing function of $\dot{\Omega}_p$ (i.e. the faster the bar slows, the smaller the adiabatic/dragged region) which implies that dynamical feedback stabilizes the bar's slowing rate.

⁵ A note on wording: This slowing rate implies $s \sim \eta/A = 0.2$ which is in the 'slow' regime ($s < 1$). However, Chiba et al. (2021) classified this model as a 'rapidly' decelerating bar in contrast to a yet slower model that evolves almost adiabatically.

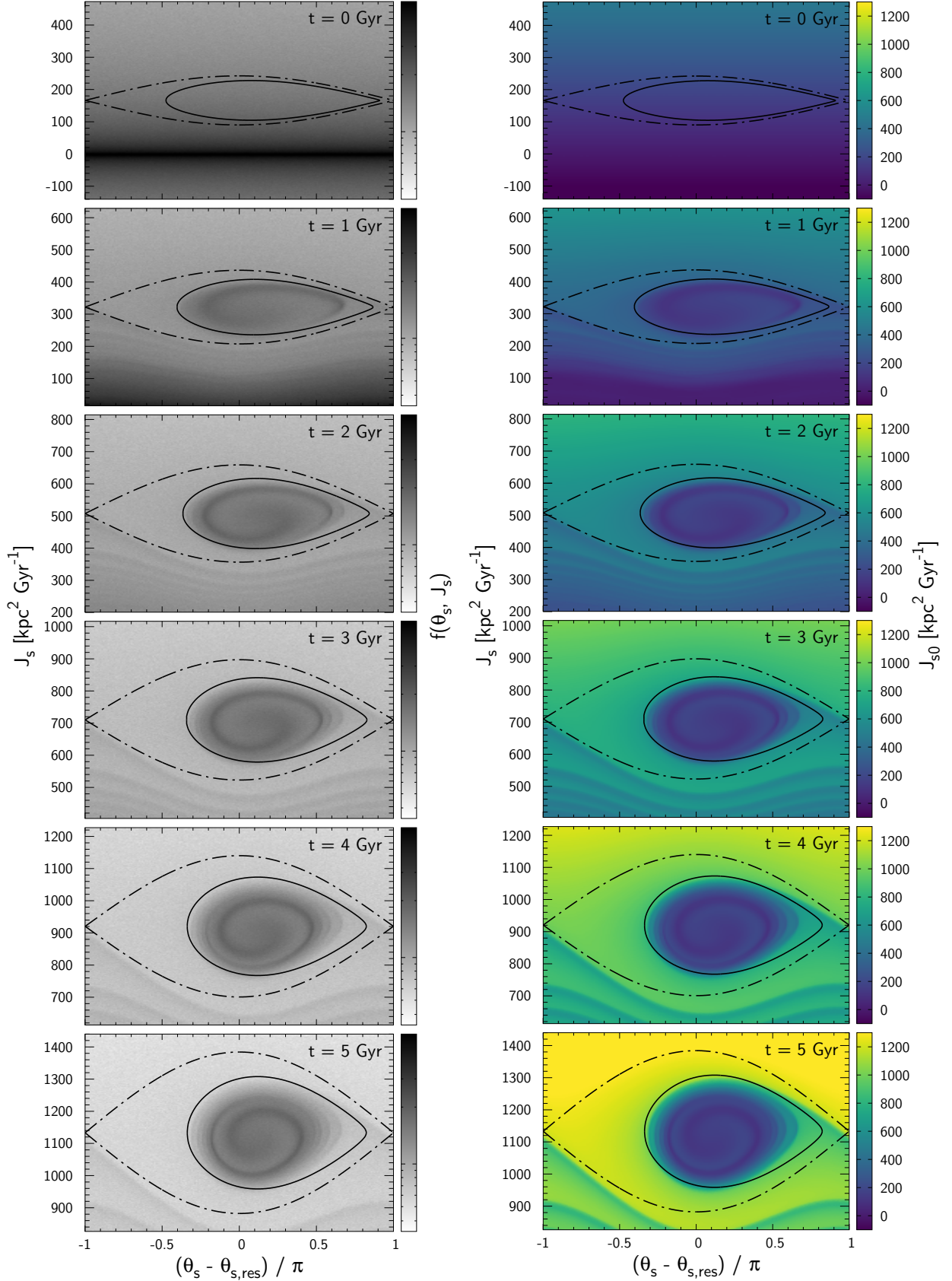


Figure 15. Time evolution of the phase-space near the CR when the bar is slowing down. The left column shows the phase-space density in log scale while the right column is coloured by the initial J_s . The phase-space spiral continues to wind up as the resonance migrates upwards (note the increasing y axis from the top panel to the bottom). The bar slows down at rate $\eta = -\dot{\Omega}_p/\Omega_p^2 = 0.004$ starting from $\Omega_p = 81.8 \text{ Gyr}^{-1}$ and ends up being $\Omega_p = 31.0 \text{ Gyr}^{-1}$ after 5 Gyr.

6 CONCLUSIONS

This work is a first attempt to push beyond the standard theory of dynamical friction that quantifies the transfer of angular momentum between galactic bars (or in fact any galactic substructures) and dark matter haloes. In particular, we have:

- shown how the standard linear perturbation theory of dynamical friction breaks down at dynamical times for bars slowing at moderate rate (the slow regime) as measured in the Milky Way,
- developed an improved description for angular momentum transfer in this slow regime by modelling the resonant dynamics using secular perturbation theory,
- shown that dynamical friction oscillates with the libration period of the main resonances, which would drive a significant fluctuation in bar pattern speed.

The standard treatment (TW84; W04) rests on the linearized collisionless Boltzmann equation: the approach assumes that the bar perturbation interacts exclusively with the pristine distribution of the halo. This assumption is valid while the perturbed distribution remains small which, in the slow regime, only holds for a few bar rotation periods. We have shown that the standard formalism reasonably predicts the angular momentum transfer directly after formation of the bar ($\lesssim 500$ Myr), but fails to predict the subsequent decay of the torque driven by the non-linear response at resonances.

When the bar forms, orbits near resonances become resonantly trapped. These trapped orbits periodically exchange z -angular momentum with the bar as they slowly librate around the resonance. For instance, orbits trapped at the corotation resonance around the stable Lagrange points have increasing angular momentum while on the trailing side of the bar and are losing angular momentum while on the leading side.

The net transfer of angular momentum to the trapped orbits is determined by their libration angle distribution: for a typical halo in equilibrium, the freshly trapped orbits are predominantly at lower angular momentum (libration angle near $\theta_\ell \sim \pi$). This phase imbalance initially leads to a net negative torque on the bar as this overdensity collectively librates up to higher angular momentum. However, after half a libration period, the overdensity starts librating back to lower angular momentum and can transfer angular momentum back to the galactic bar. Since libration periods increase towards the separatrix, this overdensity gradually winds up into a phase-space spiral inside the resonance and the net torque follows secular damped oscillations. The untrapped orbits outside the separatrix similarly exchange angular momentum with the bar as they phase mix in their circulation angle, although they have a much shorter mixing time.

We have shown that due to the near-harmonic effective potential around the resonance centre, libration periods are quite similar across the trapped volume. This provides enough coherence to cause several oscillations of the torque in the libration period. A straightforward prediction from this is that after bar formation, the pattern speed of the bar fluctuates with the typical libration frequencies of the main resonances. And indeed, while we are not aware of this having been noticed in previous literature, a closer inspection of previous N -body simulations show these predicted bar pattern speed oscillations (e.g. Aumer & Schönrich 2015, Fig.2). We also note that these oscillations in bar pattern speed take place on an order of magnitude longer timescale (> 1 Gyr) than the short-term oscillations caused by alignments between bar and spiral patterns (Wu et al. 2016; Hilmi et al. 2020).

The secular behaviour of orbits near resonances is modelled using the standard method of averaging. If the bar rotates constantly,

the averaged Hamiltonian is integrable and thus admits an angle-action coordinate for each resonance. With these new coordinates, the long-term friction can be modelled by an analytical distribution function that simply evolves in the libration/circulation angles at constant rates. The averaged Hamiltonian is, however, not accurate when neighbouring resonances lie too close: overlap of resonances leads to the onset of chaos where orbits move from one resonance to another in a stochastic manner. In our current bar model, the limited regions of chaotic phase-space did not significantly affect the estimation of the total torque, although this may not be the case with a more realistic bar with additional higher order modes (e.g. octopole).

This paper has shown qualitatively how dynamical friction may work in the slow regime. To obtain quantitative prediction, a self-consistent model is required. In particular we must model: (i) The growth of the bar which changes its effective moment of inertia. (ii) The self-gravitational perturbation of the halo which can amplify the torque on the bar by several factors (Weinberg 1989; Dootson & Magorrian 2021). (iii) The angular momentum supply from the gas which sheds angular momentum to the bar as they sink into the inner bar-region (e.g. Regan & Teuben 2004; Athanassoula et al. 2013).

Finally, the phase-space spiral predicted in this paper is also expected to form inside the resonances of the stellar disc. If we can identify this spiral pattern in the observational data, it will allow us to directly constrain the age of the Galactic bar.

ACKNOWLEDGEMENTS

It is our pleasure to thank W. Dehnen for providing us with detailed comments on our draft. We also thank J. Binney, J. Magorrian, E. Athanassoula, and M. Semczuk for many helpful comments. We in particular thank M. Weinberg for a fruitful and enlightening discussion. R.C. acknowledges financial support from the Takenaka Scholarship Foundation and the Royal Society grant RGF\R1\180095. R.S. is supported by a Royal Society University Research Fellowship. This work was performed using the Cambridge Service for Data Driven Discovery (CSD3), part of which is operated by the University of Cambridge Research Computing on behalf of the STFC DiRAC HPC Facility (www.dirac.ac.uk). The DiRAC component of CSD3 was funded by BEIS capital funding via STFC capital grants ST/P002307/1 and ST/R002452/1 and STFC operations grant ST/R00689X/1. DiRAC is part of the National e-Infrastructure.

DATA AVAILABILITY

The codes used to produce the results are available from the corresponding author upon request.

REFERENCES

- Arnol'd V. I., 1963, *Russian Mathematical Surveys*, **18**, 9
 Athanassoula E., 2003, *MNRAS*, **341**, 1179
 Athanassoula E., 2007, *MNRAS*, **377**, 1569
 Athanassoula E., Machado R. E. G., Rodionov S. A., 2013, *MNRAS*, **429**, 1949
 Aumer M., Schönrich R., 2015, *MNRAS*, **454**, 3166
 Banik U., van den Bosch F. C., 2021, arXiv e-prints, p. arXiv:2103.05004
 Binney J., 2016, *MNRAS*, **462**, 2792
 Binney J., 2018, *MNRAS*, **474**, 2706
 Binney J., 2020, *MNRAS*, **495**, 895
 Binney J., Tremaine S., 2008, *Galactic Dynamics: Second Edition*. Princeton University Press

Brizard A. J., 2013, *Commun. Nonlinear Sci. Numer. Simul.*, **18**, 511
 Ceverino D., Klypin A., 2007, *MNRAS*, **379**, 1155
 Chandrasekhar S., 1943, *ApJ*, **97**, 255
 Chiba R., Schönrich R., 2021, *MNRAS*, **505**, 2412–2426
 Chiba R., Friske J. K. S., Schönrich R., 2021, *MNRAS*, **500**, 4710
 Chirikov B. V., 1979, *Phys. Rep.*, **52**, 263
 Clarke J., Gerhard O., 2021, arXiv e-prints, p. arXiv:2107.10875
 Collett J. L., Dutta S. N., Evans N. W., 1997, *MNRAS*, **285**, 49
 Collier A., Madigan A.-M., 2021, *ApJ*, **915**, 23
 Debattista V. P., Sellwood J. A., 2000, *ApJ*, **543**, 704
 Dehnen W., 2000, *AJ*, **119**, 800
 Dootson D., Magorrian J., 2021, to be submitted
 Halle A., Di Matteo P., Haywood M., Combes F., 2018, *A&A*, **616**, A86
 Henrard J., 1982, *Celestial Mechanics*, **27**, 3
 Hernquist L., 1990, *ApJ*, **356**, 359
 Hernquist L., Weinberg M. D., 1992, *ApJ*, **400**, 80
 Hilmi T., et al., 2020, *MNRAS*, **497**, 933
 Hunt J. A. S., Bub M. W., Bovy J., Mackereth J. T., Trick W. H., Kawata D., 2019, *MNRAS*, **490**, 1026
 Kaasalainen M., 1994, *MNRAS*, **268**, 1041
 Katz D., et al., 2019, *A&A*, **622**, A205
 Lichtenberg A., Lieberman M., 1992, *Regular and Chaotic Dynamics*. Springer-Verlag
 Lynden-Bell D., Kalnajs A. J., 1972, *MNRAS*, **157**, 1
 Malhotra R., 1998, in Lazzaro D., Vieira Martins R., Ferraz-Mello S., Fernandez J., eds, *Astronomical Society of the Pacific Conference Series* Vol. 149, *Solar System Formation and Evolution*. p. 37
 Monari G., Famaey B., Fouvy J.-B., Binney J., 2017, *MNRAS*, **471**, 4314
 Monari G., Famaey B., Siebert A., Wegg C., Gerhard O., 2019, *A&A*, **626**, A41
 Petersen M. S., Weinberg M. D., Katz N., 2016, *MNRAS*, **463**, 1952
 Regan M. W., Teuben P. J., 2004, *ApJ*, **600**, 595
 Sellwood J. A., Carlberg R. G., 2014, *ApJ*, **785**, 137
 Sellwood J. A., Carlberg R. G., 2019, *MNRAS*, **489**, 116
 Sormani M. C., Binney J., Magorrian J., 2015, *MNRAS*, **454**, 1818
 Sridhar S., 2019, *ApJ*, **884**, 3
 Sridhar S., Touma J., 1996, *MNRAS*, **279**, 1263
 Tremaine S., Weinberg M. D., 1984, *MNRAS*, **209**, 729
 Trick W. H., Fragkoudi F., Hunt J. A. S., Mackereth J. T., White S. D. M., 2021, *MNRAS*, **500**, 2645
 Weinberg M. D., 1985, *MNRAS*, **213**, 451
 Weinberg M. D., 1989, *MNRAS*, **239**, 549
 Weinberg M. D., 1994, *ApJ*, **420**, 597
 Weinberg M. D., 2004, arXiv e-prints, pp astro-ph/0404169
 Weinberg M. D., Katz N., 2007, *MNRAS*, **375**, 425
 Wigner E. P., 1959, *Group Theory and Its Application to the Quantum Mechanics of Atomic Spectra*. Academic Press
 Wisdom J., 2004, *AJ*, **128**, 484
 Wu Y.-T., Pfenniger D., Taam R. E., 2016, *ApJ*, **830**, 111

APPENDIX A: DISTRIBUTION FUNCTION OF HERNQUIST HALO

The distribution function of an isotropic Hernquist halo normalized to 1 is (Hernquist 1990)

$$f(E) = \frac{1}{8\sqrt{2}\pi^3 r_s^3 v_g^3} \times \frac{3 \sin^{-1} \sqrt{\mathcal{E}} + \sqrt{\mathcal{E}(1-\mathcal{E})}(1-2\mathcal{E})(8\mathcal{E}^2 - 8\mathcal{E} - 3)}{(1-\mathcal{E})^{\frac{5}{2}}} \quad (\text{A1})$$

where $v_g = \sqrt{GM/r_s}$, and $\mathcal{E} = -E/v_g^2$ is the dimensionless binding energy. We draw initial condition for the test particles by first sampling the energy from the differential energy distribution

(Binney & Tremaine 2008)

$$N(E) = f(E)g(E) \quad (\text{A2})$$

where $g(E)$ is the density of states (i.e. phase-space volume per unit energy)

$$g(E) = \frac{2\sqrt{2}\pi^2 r_s^3 v_g}{3\mathcal{E}^{\frac{5}{2}}} \left[3(8\mathcal{E}^2 - 4\mathcal{E} + 1) \cos^{-1} \sqrt{\mathcal{E}} - \sqrt{\mathcal{E}(1-\mathcal{E})}(4\mathcal{E} - 1)(2\mathcal{E} + 3) \right]. \quad (\text{A3})$$

We then choose the initial radius r at fixed E from the distribution

$$P(r) \propto \int d^3x d^3v \delta \left[\frac{1}{2} v^2 + \Phi(x) - E \right] \delta[|x| - r] = (4\pi r)^2 \sqrt{2[E - \Phi(r)]}. \quad (\text{A4})$$

With E and r , the initial speed $v = \sqrt{2[E - \Phi(r)]}$ is determined. Finally, we pick angles randomly over a sphere in configuration space (i.e. spherical) and in velocity space (i.e. isotropic). We confirmed that the density and anisotropy distribution of test particles constructed in this manner are unaltered after 10 Gyr of iteration without perturbation by the bar.

APPENDIX B: FOURIER COEFFICIENTS OF BAR POTENTIAL

We follow the standard method of TW84, first expanding the bar's potential in spherical harmonics

$$\Phi_b(r, \vartheta, \varphi, t) = \sum_{l=0}^{\infty} \sum_{m=-l}^l \Phi_{lm}(r) Y_{lm}(\vartheta, \varphi - \Omega_p t). \quad (\text{B1})$$

For our bar model (3), only terms with $l = 2$ and $m = \pm 2$ are non-zero and their coefficients are

$$\Phi_{2,2}(r) = \Phi_{2,-2}(r) = \frac{\Phi_b(r)}{2Y_{2,2}(\pi/2, 0)}, \quad (\text{B2})$$

where $\Phi_b(r)$ is the radial profile of the bar potential (4). The Fourier coefficients $\hat{\Phi}_n(J, t)$ of the bar potential expanded in the angles $\theta = (\theta_r, \theta_\psi, \theta_\varphi)$ can then be expressed as (TW84)

$$\begin{aligned} \hat{\Phi}_n(J, t) &= \int \frac{d^3\theta}{(2\pi)^3} \Phi_b(r, \vartheta, \varphi, t) e^{-in\cdot\theta} \\ &= \sum_{l=0}^{\infty} \sum_{m=-l}^l i^{m-n_\psi} \delta_m^{n_\varphi} Y_l^{n_\psi} \left(\frac{\pi}{2}, 0 \right) d_{n_\psi m}^l(\beta) W_{lm}^{n_r n_\psi}(J) e^{-im\Omega_p t}, \end{aligned} \quad (\text{B3})$$

where $d_{n_\psi m}^l(\beta)$ is the Wigner's small d -matrix (e.g. Wigner 1959)

$$\begin{aligned} d_{n_\psi m}^l(\beta) &= \sum_t (-1)^t \frac{\sqrt{(l+n_\psi)!(l-n_\psi)!(l+m)!(l-m)!}}{(l-m-t)!(l+n_\psi-t)!t!(t+m-n_\psi)!} \\ &\quad \times \left(\cos \frac{\beta}{2} \right)^{2l+n_\psi-m-2t} \left(\sin \frac{\beta}{2} \right)^{2t+m-n_\psi}. \end{aligned} \quad (\text{B4})$$

and

$$W_{lm}^{n_r n_\psi}(J) \equiv \frac{1}{\pi} \int_0^\pi d\theta_r \Phi_{lm}(r) \cos[n_r \theta_r + n_\psi(\theta_\psi - \psi)]. \quad (\text{B5})$$

Note that $\theta_\psi - \psi$ (the azimuthal deviation from the guiding centre) only depends on θ_r for a given J , so the integral leaves no dependence on the angles. We may exert the $\delta_m^{n_\varphi}$ in (B3) and express the

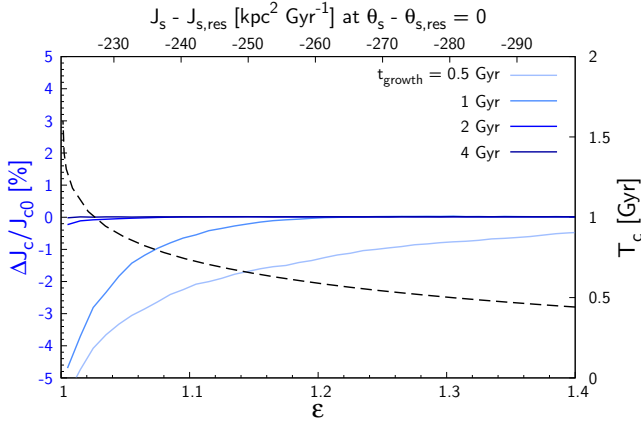


Figure C1. Changes in circulation action J_c (blue, left y-axis) at the CR as a function of ε and bar growth time t_{growth} . The black dashed curve shows the circulation period (right y-axis).

coefficients in the form of $\hat{\Phi}_{\mathbf{n}}(\mathbf{J}, t) = \hat{\Phi}_{\mathbf{n}}(\mathbf{J})e^{-in_\varphi\Omega_p t}$ where

$$\hat{\Phi}_{\mathbf{n}}(\mathbf{J}) \equiv \sum_{l=0}^{\infty} i^{n_\varphi - n_\psi} Y_l^{n_\psi} \left(\frac{\pi}{2}, 0 \right) d_{n_\psi n_\varphi}^l(\beta) W_{ln_\varphi}^{n_r n_\psi}(\mathbf{J}). \quad (\text{B6})$$

The Fourier coefficients of the bar potential expanded in the slow-fast angles $\theta' = (\theta_{f_1}, \theta_{f_2}, \theta_s)$ at resonance N are

$$\begin{aligned} \hat{\Psi}_{\mathbf{k}}(\mathbf{J}') &= \int \frac{d^3\theta'}{(2\pi)^3} \Phi_b(r, \vartheta, \varphi, t) e^{-ik \cdot \theta'} \\ &= \int \frac{d^3\theta'}{(2\pi)^3} \left[\sum_{\mathbf{n}} \hat{\Phi}_{\mathbf{n}}(\mathbf{J}) e^{i(\mathbf{n} \cdot \theta - n_\varphi \Omega_p t)} \right] e^{-ik \cdot \theta'} \\ &= \sum_{\mathbf{n}} \hat{\Phi}_{\mathbf{n}}(\mathbf{J}) \int \frac{d^3\theta'}{(2\pi)^3} \\ &\quad \times e^{i \left[(n_r - N_r \frac{n_\varphi}{N_\varphi} - k_{f_1}) \theta_{f_1} + (n_\psi - N_\psi \frac{n_\varphi}{N_\varphi} - k_{f_2}) \theta_{f_2} + \left(\frac{n_\varphi}{N_\varphi} - k_s \right) \theta_s \right]}, \end{aligned} \quad (\text{B7})$$

where the last line follows from the relation $(\theta_r, \theta_\psi, \theta_\varphi) = (\theta_{f_1}, \theta_{f_2}, (\theta_s - N_r \theta_{f_1} - N_\psi \theta_{f_2})/N_\varphi + \Omega_p t)$. Since n_φ is restricted to $m = \pm 2$, we have for resonances with $N_\varphi = 2$

$$\begin{aligned} \hat{\Psi}_{\mathbf{k}}(\mathbf{J}') &= \sum_{\mathbf{n}} \hat{\Phi}_{\mathbf{n}}(\mathbf{J}) \int \frac{d^3\theta'}{(2\pi)^3} \\ &\quad \times e^{i \left[(n_r \mp N_r - k_{f_1}) \theta_{f_1} + (n_\psi \mp N_\psi - k_{f_2}) \theta_{f_2} + (\pm 1 - k_s) \theta_s \right]} \\ &= \sum_{\mathbf{n}} \hat{\Phi}_{\mathbf{n}}(\mathbf{J}) \delta_{n_r, k_{f_1} \pm N_r} \delta_{n_\psi, k_{f_2} \pm N_\psi} \delta_{k_s, \pm 1} \\ &= \hat{\Phi}_{(k_{f_1} \pm N_r, k_{f_2} \pm N_\psi, \pm N_\varphi)}(\mathbf{J}) \delta_{k_s, \pm 1}. \end{aligned} \quad (\text{B8})$$

Therefore, the resonant term $\Psi(\mathbf{J}') \equiv 2 |\hat{\Psi}_{(0,0,1)}(\mathbf{J}')|$ in the averaged Hamiltonian (22) is

$$\Psi(\mathbf{J}') = 2 \left| \sum_{l=0}^{\infty} i^{N_\varphi - N_\psi} Y_l^{N_\psi} \left(\frac{\pi}{2}, 0 \right) d_{N_\psi N_\varphi}^l(\beta) W_{ln_\varphi}^{N_r N_\psi}(\mathbf{J}) \right|. \quad (\text{B9})$$

APPENDIX C: CONSERVATION OF CIRCULATION ACTION

Figure C1 demonstrates the conservation of circulation action J_c in our growing bar simulation presented in Fig. 5. The blue curves show the change in circulation action $\Delta J_c/J_{c0} = (J_c - J_{c0})/J_{c0}$ of

untrapped orbits in the lower circulating region for a given bar growth time t_{growth} . J_{c0} and J_c are obtained by numerically integrating the orbits' J_s over θ_s (33) before and after bar formation. We plot the mean change in J_c averaged over the final circulation angle θ_c . The x-axis ranges from $\varepsilon = 1$ (separatrix) to 1.4 and the top x-axis indicates the corresponding coordinate in $J_s - J_{s,\text{res}}$ at $\theta_s - \theta_{s,\text{res}} = 0$. The change in J_c becomes larger towards the separatrix and with shorter bar growth time. With bar growth time $t_{\text{growth}} = 4$ Gyr used in Fig. 5, most of the untrapped orbits conserve J_c to high accuracy ($< 0.1\%$). For reference, we also plot the circulation period calculated by orbit integration (black dashed, right y-axis) which is several factors smaller than the adopted t_{growth} apart from the vicinity of the separatrix.

APPENDIX D: LINEAR RESPONSE

We have shown in section 3 that standard linear perturbation theory fails to predict the torque beyond few hundred Myrs. Here we take a closer look at this issue by directly observing the linear response in the slow angle-action plane. The Fourier coefficients of the linear response (13) to a constantly rotating perturbation is

$$\begin{aligned} \hat{f}_{\mathbf{n}}(\mathbf{J}, t) &= i\mathbf{n} \cdot \frac{\partial f_0}{\partial \mathbf{J}} \int_0^t dt' e^{-i\mathbf{n} \cdot \Omega(t-t')} \left[\hat{\Phi}_{\mathbf{n}}(\mathbf{J}) e^{-in_\varphi \Omega_p t'} \right] \\ &= i\mathbf{n} \cdot \frac{\partial f_0}{\partial \mathbf{J}} \hat{\Phi}_{\mathbf{n}}(\mathbf{J}) e^{-i\mathbf{n} \cdot \Omega t} \left[\int_0^t dt' e^{i(\mathbf{n} \cdot \Omega - n_\varphi \Omega_p) t'} \right] \\ &= \mathbf{n} \cdot \frac{\partial f_0}{\partial \mathbf{J}} \hat{\Phi}_{\mathbf{n}}(\mathbf{J}) \frac{e^{-i\mathbf{n} \cdot \Omega t} - e^{-i\mathbf{n} \cdot \Omega_p t}}{\mathbf{n} \cdot \Omega - n_\varphi \Omega_p}. \end{aligned} \quad (\text{D1})$$

The total linear response is then

$$\begin{aligned} f_1(\theta, \mathbf{J}, t) &= \sum_{\mathbf{n}} \hat{f}_{\mathbf{n}}(\mathbf{J}, t) e^{i\mathbf{n} \cdot \theta} \\ &= \sum_{\mathbf{n}} \mathbf{n} \cdot \frac{\partial f_0}{\partial \mathbf{J}} \hat{\Phi}_{\mathbf{n}}(\mathbf{J}) \frac{e^{i(\mathbf{n} \cdot \theta - n_\varphi \Omega_p t)} - e^{i(\mathbf{n} \cdot \theta - \mathbf{n} \cdot \Omega t)}}{\mathbf{n} \cdot \Omega - n_\varphi \Omega_p}. \end{aligned} \quad (\text{D2})$$

Note that this equation contains the resonant frequency at the denominator but it does not diverge at the resonance because the numerator also vanishes there. From the condition that the perturbed potential is real $\hat{\Phi}_{-\mathbf{n}}(\mathbf{J}, t) = \hat{\Phi}_{\mathbf{n}}^*(\mathbf{J}, t)$, one can express f_1 as

$$\begin{aligned} f_1(\theta, \mathbf{J}, t) &= \sum_{\mathbf{n}} \mathbf{n} \cdot \frac{\partial f_0}{\partial \mathbf{J}} |\hat{\Phi}_{\mathbf{n}}(\mathbf{J})| \frac{\cos(\theta_s - \theta_{s,\text{res}}) - \cos(\theta_s - \theta_{s,\text{res}} - \Omega_s t)}{\Omega_s} \\ &= - \sum_{\mathbf{n}} \mathbf{n} \cdot \frac{\partial f_0}{\partial \mathbf{J}} |\hat{\Phi}_{\mathbf{n}}(\mathbf{J})| \sin(\theta_s - \theta_{s,\text{res}} - \Omega_s t/2) \frac{\sin(\Omega_s t/2)}{\Omega_s/2}, \end{aligned} \quad (\text{D3})$$

where $\theta_s = \mathbf{n} \cdot \theta - n_\varphi \Omega_p t$ and $\Omega_s = \mathbf{n} \cdot \Omega - n_\varphi \Omega_p$. A similar equation is presented in Weinberg & Katz (2007) (equation 15). At the resonance $\Omega_s \rightarrow 0$, the term $\sin(\Omega_s t/2)/(\Omega_s/2)$ becomes t , implying linear growth of perturbation f_1 in time. For linear theory to hold, f_1 must remain sufficiently smaller than the variation of the background distribution Δf_0 across the resonance $\Delta J_s \sim J_0 = \sqrt{-\Psi/G}$ (25). This requires

$$1 \gg \frac{f_1}{\Delta f_0} \sim \frac{\Psi}{\Delta J_s} t \sim \sqrt{-\Psi/G} t = \omega_0 t. \quad (\text{D4})$$

Hence the timescale at which linear theory is valid in the slow limit is set by the libration period $\omega_0^{-1} \gg t$.

Figure D1 compares the simulated phase flow near the corotation resonance (left) with linear perturbation theory (middle) and secular perturbation theory (right) described in section 4. Here, the libration

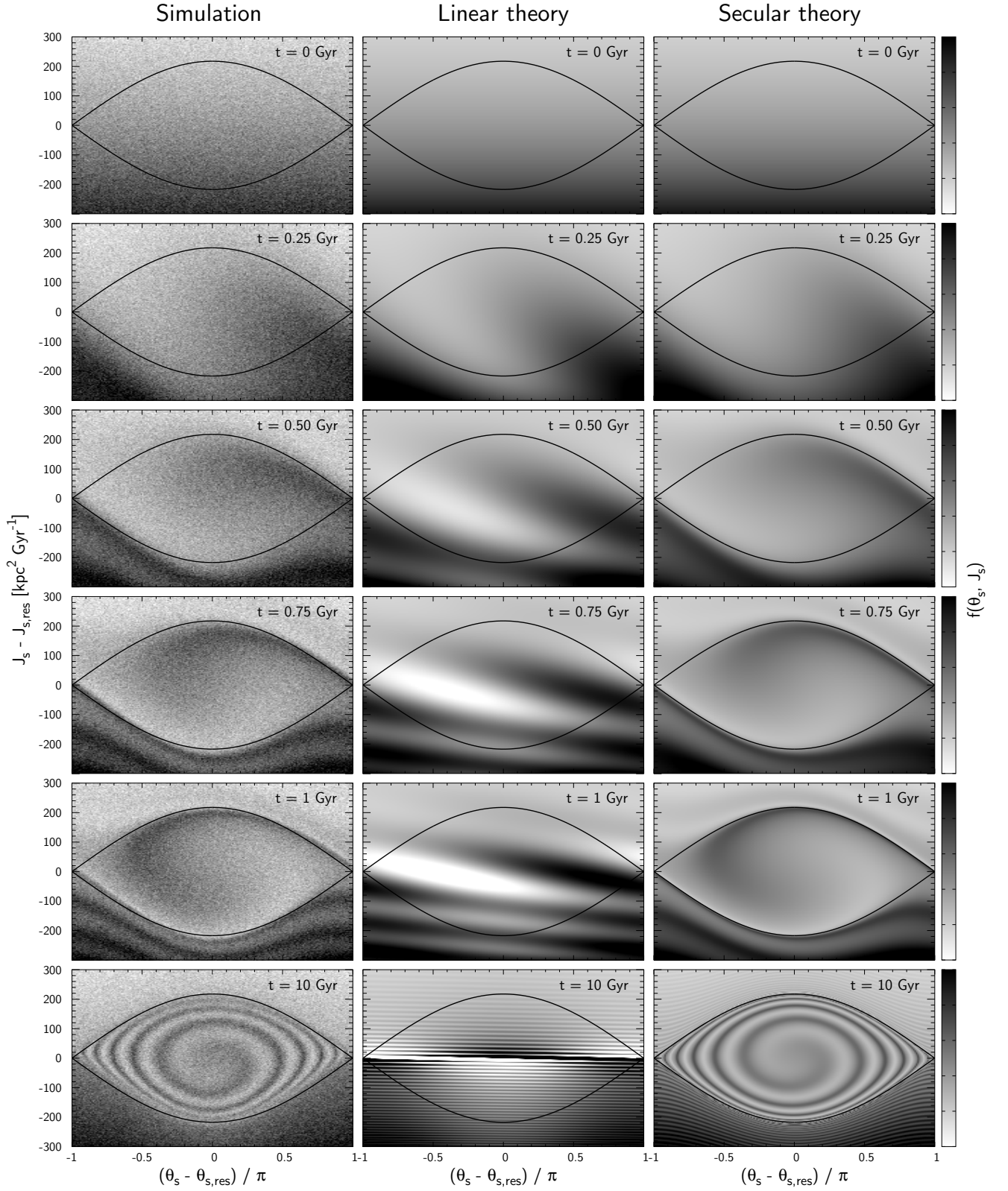


Figure D1. Comparison between simulation (left), linear perturbation theory (middle) and secular perturbation theory (right). As in Fig. 4, we show the time evolution of the phase space density near the corotation resonance at $(J_1, J_2) = (10, 0) \text{ kpc}^2 \text{ Gyr}^{-1}$. Linear theory properly predicts the phase flow for the first few hundred Myrs but fails to predict the subsequent behaviour.

period at the core of the resonance is $T_\ell = 2\pi/\omega_0 \sim 1.2$ Gyr. For the top five plots, the time since bar formation increases in steps of 0.25 Gyr, while the bottom plot shows the prediction after 10 Gyr. The linear response oscillates sinusoidally in the slow angle with phase velocities that vanish towards the resonance, as described by the term $\sin(\theta_s - \theta_{s,\text{res}} - \Omega_s t/2)$ in (D3). For the first few hundred Myrs (top two rows), this shearing motion results in a change in distribution similar to that caused by the motion of libration and circulation. However, errors in linear theory become prominent beyond $t \gtrsim 0.2T_\ell$.

Despite the growing error in linear theory, past works (e.g. Lynden-Bell & Kalnajs 1972, TW84) have commonly assumed that the perturbation was switched on in the distant past which is equivalent to taking $t \rightarrow \infty$. As noted in Weinberg & Katz (2007), in this time-asymptotic limit, the function $\sin(\Omega_s t/2)/(\Omega_s/2)$ in (D3) approaches a delta function $\pi\delta(\Omega_s/2)$ ⁶, i.e. the wavelength of the linear response in frequency (or action) space gets narrower and narrower with time, and eventually an integration over phase space will only leave contribution from the perfectly resonant orbits. This is the prediction of the LBK formula (16). This time-asymptotic limit not only ignores transient phenomena relevant in real galaxies, but also leads to qualitatively wrong conclusions: in the limit $t \rightarrow \infty$, LBK predicts that contribution from non-resonant orbits vanish by phase mixing and only the perfectly resonant orbits give rise to a *non-zero* torque, whereas in truth, the resonant orbits would also phase mix within the trapped zone resulting in a *zero* torque as shown in Fig. 1.

APPENDIX E: ELLIPTIC FUNCTIONS

The complete elliptic integral of the first $K(k)$ and second $E(k)$ kinds are defined as

$$K(k) = \int_0^{\pi/2} \frac{d\theta}{\sqrt{1 - k^2 \sin^2 \theta}}, \quad (\text{E1})$$

$$E(k) = \int_0^{\pi/2} d\theta \sqrt{1 - k^2 \sin^2 \theta}. \quad (\text{E2})$$

The incomplete elliptic integral of the first kind $F(\phi|k)$ is defined as

$$u = F(\phi|k) \equiv \int_0^\phi \frac{d\theta}{\sqrt{1 - k^2 \sin^2 \theta}}. \quad (\text{E3})$$

and the Jacobi elliptic functions are defined via the inverse of $F(\phi|k)$:

$$\phi = F^{-1}(u|k), \quad (\text{E4})$$

$$\text{sn}(u|k) \equiv \sin \phi, \quad (\text{E5})$$

$$\text{cn}(u|k) \equiv \cos \phi, \quad (\text{E6})$$

$$\text{dn}(u|k) \equiv \sqrt{1 - k^2 \sin^2 \phi}. \quad (\text{E7})$$

The derivatives of the Jacobi elliptic functions are

$$\frac{d}{du} \text{sn}(u|k) = \text{cn}(u|k) \text{dn}(u|k), \quad (\text{E8})$$

$$\frac{d}{du} \text{cn}(u|k) = -\text{sn}(u|k) \text{dn}(u|k), \quad (\text{E9})$$

$$\frac{d}{du} \text{dn}(u|k) = -k^2 \text{sn}(u|k) \text{cn}(u|k). \quad (\text{E10})$$

⁶ In the sense that,

$$\lim_{t \rightarrow \infty} \int d^3 \mathbf{J} g(\mathbf{J}) \frac{\sin(\Omega_s t/2)}{\Omega_s/2} = g(\mathbf{J}) \pi \delta(\Omega_s/2) \quad (\text{D5})$$

APPENDIX F: OVERLAP OF RESONANCES

Figure F1 overlays all three sets of resonances with $N_\psi = 2$ (black), $N_\psi = 0$ (blue) and $N_\psi = -2$ (red). As in Fig. 7, N_φ is 2 for all resonances and N_r increase from bottom left to top right: 0 to 9 (black), 1 to 10 (blue), and 2 to 11 (red). The thick solid curves mark the resonance, the dotted curve mark the maximum width of the trapped zone, and the thin lines indicate the direction of libration. All three resonances intersect near $L = 0$ where $\Omega_r = 2\Omega_\psi$ is satisfied. Overlap of bar resonances is absent at orbital inclination $\beta = 0$ (left) and $\beta = \pi$ (right), implying that chaos due to resonance overlap is of less concern in disk dynamics. At $\beta = \pi/2$ (middle), we see resonances overlapping particularly at low L and high J_r .

APPENDIX G: ORBIT SUBJECT TO A SLOWING BAR

We model an orbit trapped and dragged by a slowing bar using the Hamiltonian (22) with a time-dependent pattern speed $\Omega_p(t)$,

$$\bar{H}(\theta_s, \mathbf{J}', t) = H_0(\mathbf{J}') - N_\varphi \Omega_p(t) J_s + \Psi(\mathbf{J}') \cos(\theta_s - \theta_{s,\text{res}}). \quad (\text{G1})$$

As before, we Taylor expand around $J_s = J_{s,\text{res}}$ which satisfies the resonance condition at $t = t_{\text{res}}$:

$$\begin{aligned} \bar{H}(\theta_s, \mathbf{J}', t) \simeq & \left[H_0(\mathbf{J}') - N_\varphi \Omega_p(t) J_s \right]_{J_{s,\text{res}}} + \left[\frac{\partial H_0}{\partial J_s} - N_\varphi \Omega_p(t) \right]_{J_{s,\text{res}}} \Delta \\ & + \frac{1}{2} G(\mathbf{J}_f, J_{s,\text{res}}) \Delta^2 + \Psi(\mathbf{J}_f, J_{s,\text{res}}) \cos \theta, \end{aligned} \quad (\text{G2})$$

where we wrote $\Delta \equiv J_s - J_{s,\text{res}}$, $\theta \equiv \theta_s - \theta_{s,\text{res}}$ and $G \equiv \frac{\partial^2 H_0}{\partial J_s^2}$ for convenience. Removing the first bracket term and substituting $\frac{\partial H_0}{\partial J_s} \Big|_{J_{s,\text{res}}} = \mathbf{N} \cdot \boldsymbol{\Omega}(\mathbf{J}_f, J_{s,\text{res}}) = N_\varphi \Omega_p(t_{\text{res}})$ in the second bracket term yields (Weinberg 1994)

$$\bar{H}(\theta_s, \mathbf{J}', t) = -N_\varphi [\Omega_p(t) - \Omega_p(t_{\text{res}})] \Delta + \frac{1}{2} G \Delta^2 + \Psi \cos \theta. \quad (\text{G3})$$

From the Hamilton's equations of motion:

$$\dot{\theta} = -N_\varphi [\Omega_p(t) - \Omega_p(t_{\text{res}})] + G \Delta \quad \text{and} \quad \dot{\Delta} = \Psi \sin \theta, \quad (\text{G4})$$

we obtain

$$\ddot{\theta} + \omega_0^2 (\sin \theta - s) = 0, \quad (\text{G5})$$

where $\omega_0^2 \equiv -G\Psi$ and $s \equiv -\frac{N_\varphi \dot{\Omega}_p}{\omega_0^2}$ is the dimensionless speed parameter (TW84). If we assume that $\dot{\Omega}_p$ vary little during the typical libration period $2\pi/\omega_0$, s can be assumed constant and we obtain the following energy integral:

$$E_p = \frac{1}{2} \dot{\theta}^2 + V(\theta) \quad \text{where} \quad V(\theta) = \omega_0^2 (-\cos \theta - s\theta). \quad (\text{G6})$$

Trapped orbits are confined in the potential well of $V(\theta)$ which is linearly tilted due to the second term (see Fig.4 of Chiba et al. 2021). The crest of the potential is at $\theta_{\text{sep}} = \sin^{-1}(s)$ ($\pi/2 \leq \theta_{\text{sep}} \leq \pi$) and the minimum energy E_p required to reach the crest is

$$E_{p,\text{sep}} = \omega_0^2 (-\cos \theta_{\text{sep}} - s\theta_{\text{sep}}). \quad (\text{G7})$$

Orbit with $E_p = E_{p,\text{sep}}$ approximately marks the boundary of phase space that remains trapped in resonance. Hence, by a slight abuse of language, we will refer to the orbit $E_p = E_{p,\text{sep}}$ as the ‘separatrix’. Inserting (G7) and (G4) to (G6) yields an equation for the separatrix:

$$\Delta_{\pm} = \frac{N_\varphi [\Omega_p(t) - \Omega_p(t_{\text{res}})]}{G} \pm \frac{\omega_0}{G} \sqrt{2 [\cos \theta - \cos \theta_{\text{sep}} + s(\theta - \theta_{\text{sep}})]}. \quad (\text{G8})$$

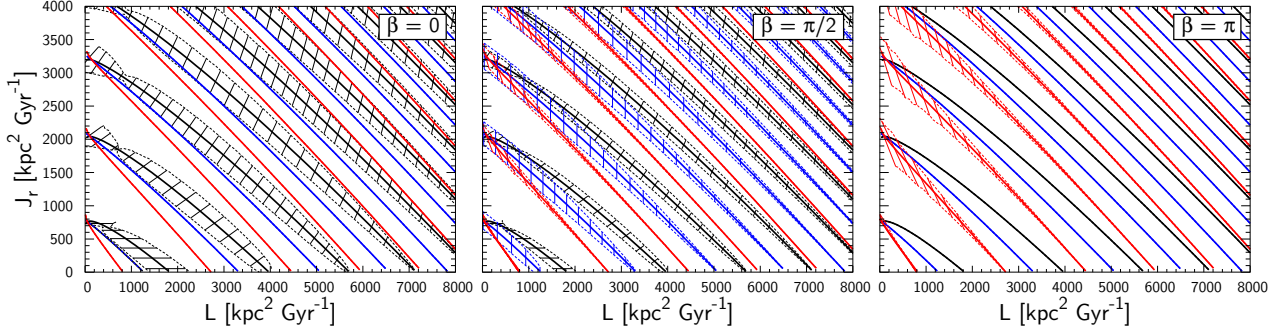


Figure F1. Overlap of resonances with $N_\psi = 2$ (black), $N_\psi = 0$ (blue) and $N_\psi = -2$ (red). See text for detail.

The first term describes the movement of the resonance since t_{res} and the second term describes the shape of the separatrix. Since the first term is time dependent, the separatrix is not closed in phase space. However, in the slow limit $s \ll 1$ the distance the resonance travels in a typical libration period is smaller than the size of the resonance, so we may mark the approximate area of trapped phase space by neglecting the first term. This is drawn in Fig. 15. In comparison to the separatrix of the time-frozen Hamiltonian (dot-dashed black), the separatrix of the time-dependent Hamiltonian (solid black) is contracted and shifted towards θ , describing the trapped boundary of the simulation remarkably well. The first term in fact breaks/opens the separatrix and thus allows orbits to enter or escape the trapped region.

Setting $s = 0$ in equation (G8), we recover the equation for the separatrix of a standard pendulum Hamiltonian (e.g. [Lichtenberg & Lieberman 1992](#)):

$$\Delta_{\pm} = \pm \frac{2\omega_0}{G} \cos \frac{\theta}{2}. \quad (\text{G9})$$

This paper has been typeset from a \LaTeX file prepared by the author.